Lund University

Faculty of Engineering

Division of Mechanics

Master Thesis in the Field of Mechanical Engineering

Quantification and Implementation of Structural Damping in MBS Flexible Bodies

Author:
Anton Flink

Supervisors:
Anders Ahlström
Kristina Nilsson

June 2015

Abstract

In multi body simulation (MBS) using flexible bodies, damping is an important model input to be able to predict the response of a structure with sufficient precision. The purpose of this thesis has been to estimate the structural damping of an experimental setup and implement the estimated damping into MBS-models of the setup.

In this thesis the modal properties in terms of natural frequencies, mode shapes and modal damping of a chassis frame with a number of attached components are identified through physical testing. The experimental setup is modeled in the MBS software MSC Adams using both flexible and rigid bodies coupled together, a total of three different models are created. Two with different modeling of the bolted joints in the setup and one where components are modeled as separate flexible bodies and coupled with joints. The modal properties of the models are compared to the identified modal properties of the setup.

The simplification in modeling of the bolted joints results in small differences in modal properties of the model compared to more detailed modeling of the bolted joints. Modeling of components as separate flexible bodies results in lesser consistency compared to identified modal parameters, making it more difficult to mimic the damping of the experimental setup.

For each of the models a damping function is suggested and implemented,based on the identified modal damping of the physical system. Simulation is then performed, comparing the different models ability to predict the pseudo damage relative to the physical system.

The suggested damping functions shows improved ability to predict pseudo damage for components attached to the chassis frame. The prediction of pseudo damage on the frame side members and cross members is less sensitive to the choice of damping in the MBS-model. Parts of the modeling procedure as well as the implementation of identified damping shows room for improvement and further studies are recommended.

Acknowledgements

I would like thank the people involved in this project for valuable help and guidance. Firstly my supervisor at Scania, Anders Ahlström for making this possible and providing useful guidance and knowledge.

I would also like to thank Ulrika Lagerblad, Ph.D. student at RTCC, and Martin Linderoth, RTRD, for providing help with the experimental part of the thesis. Rickard Österlöf, Ph.D. student at RTCC, is also acknowledged for useful discussions and ideas.

Moreover, I am very grateful for all support provided from the coworkers at RTCC, both in terms of help related to the project and great company during numerous coffee breaks.

Lastly I would like to express my thanks to my supervisor at LTH, Krisitna Nilsson, for providing feedback and critical reviewing of the thesis.

Contents

1 Introduction

1.1 Background

Heavy vehicle manufacturer Scania CV AB is continuously working towards improving product properties such as comfort and handling. Evaluation of vehicle properties is done both through physical testing and virtual simulation. Physical testing of the vehicle is time consuming and cannot be done early in the development process. Therefore virtual simulation serves as a powerful tool to evaluate properties in early stages of the development process. However, knowledge of the simplifications and limitations involved in modeling is crucial to obtain useful results through simulation. This includes knowledge and correct modeling of structural damping in the system.

Multi body simulation (MBS) is used at Scania CV AB to evaluate comfort and handling properties of the vehicle. The MBS model can consist of rigid and/or flexible bodies connected through different types of joints and force elements. For flexible bodies the structural damping is an important input to the model. The damping can be set individually for each mode of the flexible body.

1.2 Aim

The aim of this thesis is to:

- Estimate structural damping through measuring the response of an experimental setup.
- Modeling of the same experimental setup in MBS software.
- Finding suitable ways of implementing estimated damping data into the MBS model of the experimental setup.
- Verification of the MBS model with implemented damping through simulation and comparison to measurement.

1.3 Methodology

The estimation of the structural damping in the structure is based on the method of experimental modal analysis (EMA), which aims to determine the modal properties such as natural frequencies, mode shapes and modal damping of an experimental setup subject to excitation and measurement of the response. The modal parameter estimation is conducted using the commercial software LMS Test.Lab Modal Analysis.

Modeling of the experimental setup is done in the MBS-software MSC Adams. The created models consists of both rigid and flexible bodies. The flexible bodies are based on condensed FE-models created in the software HyperMesh and generated in the FE-solver software Abaqus.

The implementation was based on the possibility to set a unique modal damping for each mode of the flexible body in MSC Adams. Upon searching the literature no information on this specific topic was found. Previously at Scania the subject of damping in flexible bodies has been investigated, e.g. in [18] and [19], however in these cases the choice of modal damping is not based on estimations of the damping of the physical system.

To evaluate the performance of the models with the implemented damping their ability to predict the pseudo damage relative the experimental setup is investigated. The calculation of pseudo damage is based on theory of fatigue in materials. In the design of heavy vehicles fatigue is one of the most important design factors, hence the choice of calculating pseudo damage.

1.4 Delimitations

The work in this thesis is limited to the study of one experimental setup. The estimated modal parameters are based on a single amplitude white noise excitation. The modeling of damping is limited to using a linear viscous damping model. No full vehicle simulation is conducted to further evaluate results obtained in the study.

2 Theory

2.1 Damping

The dissipation of energy from a mechanical system is referred to as the damping of the system. In most cases the mechanical energy is transformed to heat. There are usually numerous sources of damping and the mechanisms considered to be of interest for the scope of this work will be briefly described together with references for a more thorough description.

- Material damping:
  Material damping, also often referred to as hysteretic damping is energy dissipation within the material, e.g. internal friction due to internal rearrangement such as dislocations in the material. The material damping is hard to analyze theoretically due to the different underlying mechanisms, it also shows a nonlinear behaviour w.r.t for example strain amplitude in the material. Even though the physics behind material damping makes it hard to model, the energy dissipation associated with it can be determined through cyclic loading by measuring stress and strain during load cycles and estimating energy loss through the hysteresis loop. In general for materials such as steel, the material damping is of little significance compared to other sources of damping such as damping occurring in joints in the structure, however rubber materials may be associated with high energy dissipation. Material damping and modeling of material damping is further discussed in Bert [1],Beards [2] and Gaul [3].

- Damping in bolted joints:
  Damping in bolted joints involve three different energy dissipation mechanisms. These are: macro slip, i.e. relative motion between the surfaces at the interface of the joint, micro slip, small relative motion between irregularities of the interface surfaces and local plastic deformation of surface irregularities due to high contact pressure. All of the described mechanisms are present in a bolted joint, though their relative impact on the dissipated energy is highly dependent on the clamping pressure. At lower pressure macro slip is dominant and at higher pressure the plastic deformation is the dominant mechanism. These mechanisms are described more in detail in Beards [2]. Xu & Hess [4], examined the effect of preloading in a bolted joint with respect to natural frequencies and modal damping and found that at low preloads the modal damping increases heavily, whereas at higher levels it remains relatively constant. Wentzel [5] suggests a numerical method for estimating the damping in a bolted joint through FE-simulation and shows that damping in bolted joints can be well estimated through simulation.

- Viscous damping:
  Although not directly present in many mechanical systems, viscous damping has been of great importance for modeling of mechanical systems. The classical example of viscous damping is the dashpot, a mechanical device containing a piston moving in a fluid in a confined space. The dashpot damper will generate force proportional to the velocity of the motion, acting in the opposite direction. Damping of mechanical systems is often modeled using the dashpot and viscous damping. Even though viscous damping may not be present, the viscous damping model provides simplicity and ease of analysis of the system. If the source of damping is of another type an *equivalent viscous damping* can be calculated to represent the same energy dissipation per cycle. The concept of equivalent viscous damping is further discussed by Hudson [6].

2.2 Modal analysis

A mechanical system can be described by its inertia, stiffness and damping properties. Inertia and stiffness properties of a system can be determined easily using FE-modeling given the geometry and material properties of the system, damping is however harder to determine. Modal analysis aims to describe the dynamics of a system in terms of natural modes, where each mode has a corresponding mode shape, natural frequency and modal damping. Using this concept allows for decoupling of the equations of motions of the system, hence any motion of the system can be described by a linear combination of the systems natural modes. The decoupling of the equations of motion opens up the possibility to reduce the model size through modal truncation. Combined with modal testing, which is an experimental procedure through which the mode shapes, natural frequencies and damping ratios can be determined, modal analysis can be used to correlate and correct a FE model using experimental data.[7]

Consider the harmonic motion of the undamped multiple degree of freedom (MDOF) mechanical system described by:

$$\mathbf{M}\ddot{\mathbf{x}} + \mathbf{K}\mathbf{x} = \mathbf{0} \tag{1}$$

where $\mathbf{M}$ denotes the mass matrix, $\mathbf{K}$ the stiffness matrix, $\mathbf{x}$ the displacement vector and dot represents differentiation with respect to time. Assuming a solution of the form:

$$\mathbf{x} = \mathbf{X}_i \sin \omega_i t \tag{2}$$

where $\mathbf{X}_i$ denotes the mode shape, ω_i the natural frequency, and t time. Combining (1) and (2) we obtain:

$$(\mathbf{K} - \omega_i^2 \mathbf{M})\mathbf{X}_i = \mathbf{0} \tag{3}$$

which is an n:th order eigenvalue problem for the system with n degrees of freedom. Solving the eigenvalue problem we obtain n eigenfrequencies ω_i with corresponding eigenvectors $\mathbf{X}_i$ where $i = 1, 2, 3, ..., n$. Given that the eigenvalues of the system are distinct, the mode shapes, i.e. the eigenvectors will be orthogonal with respect to the mass and stiffness matrices. Orthogonality will yield the following properties for the mass and stiffness matrices:

$$\mathbf{X}_i^T \mathbf{M} \mathbf{X}_j = \begin{cases} 0, & \text{if } i \neq j \\ m_i, & \text{if } i = j \end{cases} \quad \mathbf{X}_i^T \mathbf{K} \mathbf{X}_j = \begin{cases} 0, & \text{if } i \neq j \\ k_i, & \text{if } i = j \end{cases}. \tag{4}$$

Normalizing the eigenvectors by setting $m_i = 1$ will result in $k_i = \omega_i^2$, which is referred to as mass normalization of the mode shapes. Arranging the mode shapes in a modal matrix with the mode shapes as columns yields:

$$\mathbf{\Psi} = [\mathbf{X}_1, \mathbf{X}_2, \mathbf{X}_3, ..., \mathbf{X}_n,]. \tag{5}$$

Using this we can transform the physical coordinates to the modal coordinates $\mathbf{q}$ through:

$$\mathbf{x} = \mathbf{\Psi}\mathbf{q}. \tag{6}$$

Forced vibration of an undamped MDOF system can then be described by:

$$\mathbf{M}\mathbf{\Psi}\ddot{\mathbf{q}} + \mathbf{K}\mathbf{\Psi}\mathbf{q} = \mathbf{F}(t) \tag{7}$$

where $\mathbf{F}(t)$ is the time varying external force vector. Premultiplying by $\mathbf{\Psi^T}$ we obtain:

$$\mathbf{\Psi^T M \Psi \ddot{q}} + \mathbf{\Psi^T K \Psi q} = \mathbf{\Psi^T F}(t) \tag{8}$$

which can be rewritten as:

$$\hat{\mathbf{M}}\ddot{\mathbf{q}} + \hat{\mathbf{K}}\mathbf{q} = \hat{\mathbf{F}}(t) \tag{9}$$

and reconsidering (4) we conclude that the equations of motion has been successfully decoupled since both the modal mass matrix $\hat{\mathbf{M}}$ and the modal stiffness matrix $\hat{\mathbf{K}}$ are diagonal matrices. The above procedure can be applied on a viscously damped MDOF system described by:

$$\mathbf{M}\ddot{\mathbf{x}} + \mathbf{C}\dot{\mathbf{x}} + \mathbf{K}\mathbf{x} = \mathbf{F}(t). \tag{10}$$

However it will not yield a diagonal modal system for arbitrary damping matrices $\mathbf{C}$. For special choices of the damping matrix the system can be successfully diagonalized. The most common choice known as Rayleigh damping or proportional damping, suggested by Rayleigh[8], defines the damping matrix as a linear combination of the mass matrix and stiffness matrix according to:

$$\mathbf{C} = \alpha\mathbf{M} + \beta\mathbf{K} \tag{11}$$

where α and β are constants. For each of the uncoupled equations we can now define a modal damping ratio, which can be expressed as fraction of critical damping for each mode. Rayleigh damping will result in certain modal damping ratios. Study the equation of motion for the i:th mode:

$$m_i\ddot{q}_i + c_i\dot{q}_i + k_i q_i = 0 \tag{12}$$

where m_i denotes the modal mass, c_i the modal damping and k_i the modal stiffness. Assuming a solution of the form $q_i = e^{rt}$ we obtain the characteristic equation:

$$m_i r^2 + c_i r + k_i = 0. \tag{13}$$

Solving for r we obtain:

$$r = \frac{-c_i \pm \sqrt{c_i^2 - 4k_i m_i}}{2m_i}. \tag{14}$$

For $c_i^2 - 4k_i m_i < 0$ the solution will be a harmonic decay, for $c_i^2 - 4k_i m_i > 0$ the solution will take the form of a steady decay with no harmonic part. The critical damping c_i^{cr} is the value of c_i for which $c_i^2 - 4k_i m_i = 0$, resulting in:

$$c_i^{cr} = 2\sqrt{k_i m_i}. \tag{15}$$

The critical damping ratio for mode i, ξ_i, can then be expressed as:

$$\xi_i = \frac{c_i}{c_i^{cr}} \tag{16}$$

allowing us to express the modal damping ratio c_i in terms of the critical damping ratio, modal mass and modal stiffness:

$$c_i = 2\xi_i\sqrt{k_i m_i}. \tag{17}$$

This allows us to apply a modal damping for each mode, without having to specify any damping for the system in the physical coordinates. Having knowledge

of the modal damping from testing then allows for the measured damping to be applied in the model.

Using that the system is diagonal it can now be truncated to retain only m degrees of freedom, $m < n$. This is especially useful for reducing problem size in dynamic analysis. Knowing the frequency span of the external forces acting on the system, modes with eigenfrequencies far away from the span of interest can be successfully removed without impacting the result of the analysis [9].

2.3 Craig-Bampton reduction

As described above modal analysis is useful for dynamic simulations of mechanical systems. However in multi body simulation (MBS), the system can consist of many different substructures, rigid or flexible, coupled together at common boundary points, also known as interface nodes. For this purpose the modal basis has been proved inadequate [9] which led to the development of component mode synthesis (CMS) used for dynamic analysis of systems consisting of different coupled substructures. The Craig-Bampton method is a commonly used CMS method and will be introduced below.

Consider again the system described by:

$$\mathbf{M}\ddot{\mathbf{x}} + \mathbf{K}\mathbf{x} = \mathbf{F}(t). \tag{18}$$

Instead of transforming the whole system to the modal basis, we first partition the system into interior coordinates $\mathbf{x}_I$ and boundary coordinates $\mathbf{x}_B$:

$$\begin{bmatrix} \mathbf{M}_{BB} & \mathbf{M}_{BI} \\ \mathbf{M}_{IB} & \mathbf{M}_{II} \end{bmatrix} \begin{bmatrix} \ddot{\mathbf{x}}_B \\ \ddot{\mathbf{x}}_I \end{bmatrix} + \begin{bmatrix} \mathbf{K}_{BB} & \mathbf{K}_{BI} \\ \mathbf{K}_{IB} & \mathbf{K}_{II} \end{bmatrix} \begin{bmatrix} \mathbf{x}_B \\ \mathbf{x}_I \end{bmatrix} = \begin{bmatrix} \mathbf{F}_B \\ \mathbf{F}_I \end{bmatrix}. \tag{19}$$

Where the subscripts I and B denotes interior and boundary respectively, e.g. the mass matrix M_{BB} describes mass coupling in-between boundary DOF:s and M_{IB} mass coupling between interior and boundary DOF:s. The boundary degrees of freedom (DOF:s) will not undergo any transformation, they will remain the same in the Craig-Bampton basis. The interior DOF:s will be described as a combination of two different types of mode shapes, the constraint modes, which are obtained by giving each boundary DOF a unit displacement, and the fixed boundary normal modes which are obtained by fixating the boundary DOFs and computing the eigensolution for the interior DOF:s:

$$(\mathbf{K}_{II} - \omega^2 \mathbf{M}_{II})\mathbf{X}_{II} = \mathbf{0}. \tag{20}$$

Performing truncation and retaining the m desired modes we now obtain the interior normal modes matrix:

$$\mathbf{\Psi_I} = [\mathbf{X}_{II1}, \mathbf{X}_{II2}, \mathbf{X}_{II3}, ..., \mathbf{X}_{IIm},]. \tag{21}$$

If we also calculate the constraint modes modal matrix $\mathbf{\Psi_B}$ through assuming zero inertia effects for the static modes and prescribing a unit displacement for each boundary DOF, we refer to [10] for the details, we obtain the Craig-Bampton transformation matrix relating the physical coordinates to the coordinates in the Craig-Bampton basis:

$$\begin{bmatrix} \mathbf{x}_B \\ \mathbf{x}_I \end{bmatrix} = \begin{bmatrix} \mathbf{I} & \mathbf{0} \\ \mathbf{\Psi}_B & \mathbf{\Psi}_I \end{bmatrix} \begin{bmatrix} \mathbf{q}_B \\ \mathbf{q}_I \end{bmatrix} = \mathbf{\Psi_{CB}}\mathbf{q_{CB}} \tag{22}$$

where I denotes the identity matrix. Substituting (22) into (18) and premultiplying with the transpose of the transformation matrix in (22), which we will now denote $\mathbf{\Psi}_{CB}^{T}$, we obtain the Craig-Bampton reduction of the original system:

$$\mathbf{\Psi_{CB}^{T}M\Psi_{CB}\ddot{q}_{CB}} + \mathbf{\Psi_{CB}^{T}K\Psi_{CB}q_{CB}} = \mathbf{\Psi_{CB}^{T}F}(t). \tag{23}$$

Which we can rewrite to:

$$\mathbf{M_{CB}\ddot{q}_{CB}} + \mathbf{K_{CB}q_{CB}} = \mathbf{F_{CB}}(t). \tag{24}$$

Where $\mathbf{K_{CB}}$ now is a block diagonal matrix and the blocks of $\mathbf{M_{CB}}$ and $\mathbf{K_{CB}}$ associated with eigenvectors $\mathbf{\Psi_I}$ are diagonal. The Craig-Bampton method allows for reduction of the problem size while still retaining interface nodes to enable coupling with other substructures. Using proportional damping as discussed in the previous section, the Craig-Bampton method also holds for viscously damped systems.

2.4 The MSC Adams flexible body

The Craig-Bampton reduction provides a reduced model, capturing dynamic content of the system as well as allowing for coupling with other substructures. However, for a number of reasons mentioned in [9], the Craig-Bampton basis is not optimal for successful dynamic simulation in MSC Adams, these reasons being:

- The Craig-Bampton modes contains six rigid body modes which needs to be eliminated as Adams provides the rigid body DOF:s.
- The constraint modes are obtained from static condensation and hence does not have a natural frequency related to them.
- Disabling constraint modes is equivalent to applying a constraint on the system.

This problem is solved by orthogonalizing the Craig-Bampton system through solving the eigenvalue problem:

$$(\mathbf{K_{CB}} - \lambda^2\mathbf{M_{CB}})\mathbf{X_{CB}} = \mathbf{0} \tag{25}$$

and then arranging the eigenvectors into a transformation matrix $\mathbf{T}$, allowing us to transform the system to an orthogonal basis using $\mathbf{q_{CB}} = \mathbf{Tq^{o}}$:

$$\mathbf{T^{T}M_{CB}T\ddot{q}^{o}} + \mathbf{T^{T}K_{CB}Tq^{o}} = \mathbf{T^{T}F}(t) \tag{26}$$

The transformation yields a diagonal system. Static constraint modes are now transformed into boundary eigenvectors with associated eigenfrequency, the fixed boundary normal modes are transformed into modes approximating the unconstrained modes of the system and finally a set of modes are obtained that cannot be interpreted in terms of physical eigenvectors. This solves the problems mentioned above:

- The diagonal system contains six rigid body modes, which can now be successfully disabled.
- All modes now have a frequency associated with them, removing the problem with static constraint modes.
- Boundary modes can now be disabled without applying constraints to the system, removing boundary modes will however prevent the boundary from adopting certain shapes.

The obtained linear system is used to describe flexible bodies in MSC Adams, and is suitable for use in dynamic MBS. The modal damping for the flexible body can now be set individually for each mode as the fraction of critical damping described in (17).

2.5 EMA - Experimental modal Analysis

As explained in Section 2.2, modal analysis can be used to decouple the equations of motion and describe a system in terms of dynamic properties such as natural frequencies, mode shapes and modal damping. The purpose of modal testing and EMA, is to identify the dynamic properties through exciting a system and measure the input excitation and the output response of the system. The input and output data are used to create frequency response functions (FRFs) to which a modal model is fitted by estimating the modal parameters of the system. There are numerous methods for estimating modal parameters, this section will introduce the basics of EMA and the method used in this work.

2.5.1 Frequency response functions - FRFs

For a single degree of freedom (SDOF) system as depicted in Figure 1a exposed to a harmonic force the equation of motion is given by:

$$m\ddot{x} + c\dot{x} + kx = f(t). \tag{27}$$

Using that:

$$\frac{c}{m} = 2\xi\omega_{nat}, \qquad \frac{k}{m} = \omega_{nat}^2 \tag{28}$$

where nat denotes the natural frequency,and dividing by m the following is obtained:

$$\ddot{x} + 2\xi\omega_{nat}\dot{x} + \omega_{nat}^2 x = \frac{f(t)}{m}. \tag{29}$$

Taking the Fourier transform of both sides then results in:

$$X(-\omega^2 + j2\xi\omega_{nat}\omega + \omega_{nat}^2) = \frac{F(\omega)}{m} \tag{30}$$

where j is the imaginary unit $j = \sqrt{-1}$. The FRF $H(\omega)$ for the system is defined as the relation between the input force and output displacement:

$$H(\omega) = \frac{X(\omega)}{F(\omega)} = \frac{1}{m}\frac{1}{-\omega^2 + j2\xi\omega_{nat}\omega + \omega_{nat}^2} \tag{31}$$

where $X(\omega)$ is the displacement and $F(\omega)$ the external force. It is evident from (31) that the obtained FRF contains the modal parameters of the system. The same procedure can be repeated for a SDOF system exposed to harmonic base excitation as depicted in Figure 1b.

Different FRFs will then be obtained for the relation between the absolute displacements and for the relation between the relative displacement $z(t) = (x(t) - y(t))$ and the base:

$$\begin{aligned} H(\omega) &= \frac{X(\omega)}{Y(\omega)} = \frac{j2\xi\omega_{nat}\omega + \omega_{nat}^2}{-\omega^2 + j2\xi\omega_{nat}\omega + \omega_{nt}^2} \\ H(\omega) &= \frac{Z(\omega)}{Y(\omega)} = \frac{-1}{-\omega^2 + j2\xi\omega_{nat}\omega + \omega_{nat}^2} \end{aligned} \tag{32}$$

Note that the FRFs in (32) also contains the modal parameters. The FRFs can also be calculated between output velocities or accelerations with respect to input

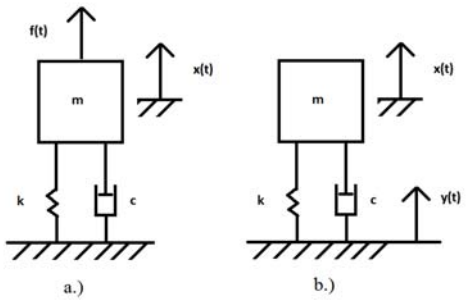

Figure 1: SDOF system excited by a harmonic force $f(t)$ to the left and harmonic base excitation $y(t)$ to the right.

displacement, velocity, acceleration or force. Considering an MDOF system with m inputs and n outputs, note how indexes m and n now changes meaning, a mxn matrix of FRFs $\mathbf{H}$ will relate the input to the output, each position in the FRF matrix given by:

$$H_{mn}(\omega) = \frac{B_n(\omega)}{A_m(\omega)} \Rightarrow \mathbf{H}(\omega)\mathbf{A}(\omega) = \mathbf{B}(\omega) \tag{33}$$

where A denotes the input and B the output.

2.5.2 FRF estimators

Given a set of measured input and output time histories, the FRFs can be calculated using several different methods, known as FRF estimators. The purpose of these estimators is to reduce the impact of the noise present during measurements, hence these estimators are used rather than analytical expressions as in Section 2.5.1. Three commonly used estimators are H_1, H_2 and H_v which are described below. H_1 serves to reduce noise on the output signal and is defined as:

$$H_1 = \frac{G_{xf}}{G_{ff}} \tag{34}$$

where G_{xf} is the cross power spectrum of the input signal f and output signal x and G_{ff} the auto power spectrum of f. The auto power spectrum of a signal is the cross correlation between a signal and itself and describes the energy of the signal as a function of frequency. The cross power spectrum between two signals shows the power shared between the signals as a function of frequency. The H_2 estimator reduces the impact of noise on the input signal and is defined as:

$$H_2 = \frac{G_{xx}}{G_{fx}}. \tag{35}$$

Finally the H_v estimator can be used when noise in present both on the input and output signal. H_v is calculated through eigenvalue decomposition of a matrix of different power spectrums. The details of the calculation are left to [11]. However for the single input single output case it simplifies to:

$$H_v = \frac{G_{xf}}{\mid G_{xf} \mid} \sqrt{\frac{G_{xx}}{G_{ff}}}. \tag{36}$$

2.5.3 Estimation of modal parameters

Given a set of estimated FRFs from measurement, the goal of modal parameter estimation is to find the best fit of the modal model to the experimental data. The modal parameters to be fitted are λ_k, which contains the undamped natural frequency and the modal damping ratio, and r_{mnk}, which contains the mode shape coefficients. For the MDOF system given in (33) the FRF in (31) can be generalized to:

$$H_{mn}(j\omega) = \sum_{k=1}^{N} \left(\frac{r_{mnk}}{j\omega - \lambda_k} + \frac{r^*_{mnk}}{j\omega - \lambda^*_k} \right) \tag{37}$$

where N is the number of modes, r_{mnk} the residue value of mode k, λ_k the pole value for mode k and $*$ denotes the complex conjugate. The pole value λ contains the undamped natural frequency ω_k and damping ratio ξ_k of the mode.The residue contains the mode shape coefficients, v_{mk} and v_{nk} for the reference and response FRF used, as well as a complex scaling constant a_k:

$$\lambda_k = -\xi_k \omega_k + j\omega_k \sqrt{1 - \xi_k^2}, \qquad r_{mnk} = a_k v_{mk} v_{nk}. \tag{38}$$

In general the force is the measured quantity at the reference point m, however it has been shown in Beliveau et. al [12] that modal parameters can be successfully identified measuring acceleration at both reference and response locations. In Bergström [13] modal parameters are successfully identified by creating acceleration based FRFs and is also further used in Wentzel [5].

In equation 37 it is assumed that the system has N number of modes. In reality the number of modes of the system is unknown, since the purpose of the procedure is to identify the modes of the system in a certain frequency range. This issue is solved through usage of stabilization diagrams. By estimating the modal parameters for an increasing number of modes, a stabilization diagram can be obtained as seen in Figure 2. The diagram plots the sum of the used FRFs together with the identified modes for increasing model size N. Modes that reoccur at the same frequency with the same damping as N increases can then be interpreted as physical modes of the system. The physical modes of the system should not change with model size. The other modes are known as computational modes and arise due to the curve fitting procedure.

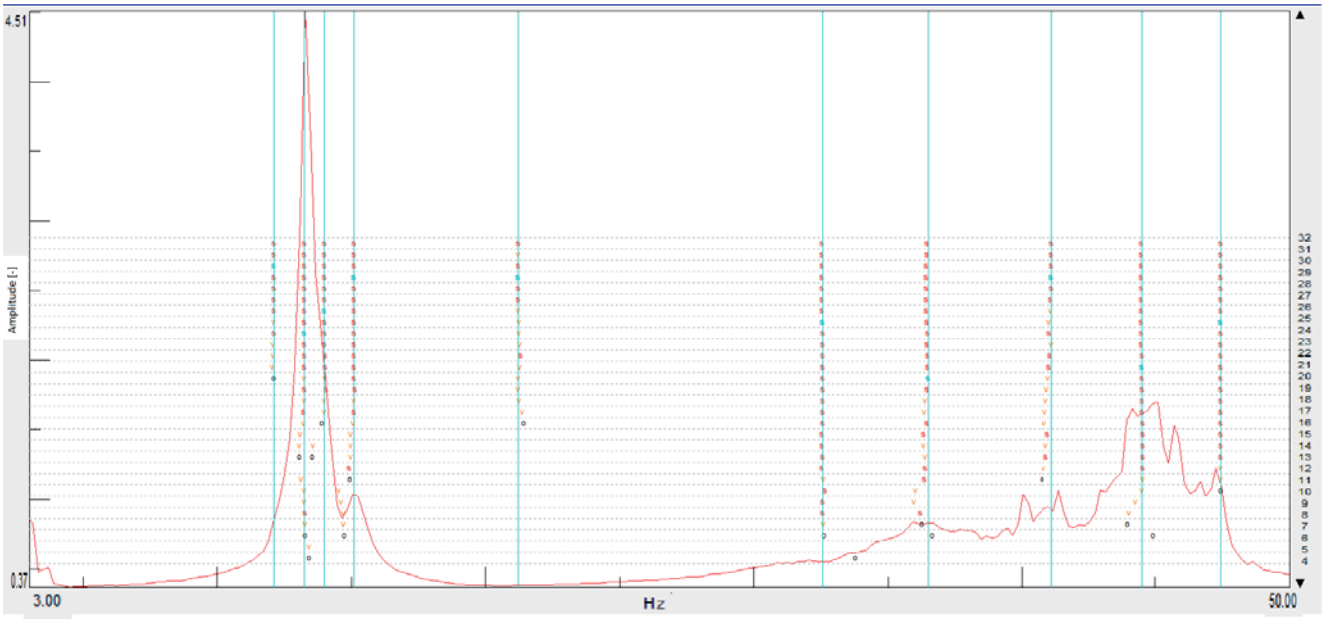

Figure 2: Stabilization diagram. The red curves shows the sum of used FRFs, model size N is indicated on the right hand side, s (red symbol) denotes stable reoccurring modes. The x-scale shows frequency in Hz and the y-scale the amplitude of the FRF, in this case dimensionless.

A number of different estimation algorithms can be used to perform the modal parameter estimation. In general, these can be categorized based on three different properties:

- **MDOF/SDOF**
  For systems with well separated modes, each mode within a specific frequency band can the treated as a SDOF system. By adding residual terms neighbouring modes can be compensated for. If modes are closely coupled the SDOF methods will not provide good estimates. MDOF methods then have to be used which estimates parameters for several modes simultaneously.

- **Local/Global**
  Local methods estimates modal parameters for each FRF, ignoring the others. This yields as many estimated parameters for each mode as the number of FRFs. It is then up to the user to in some manner choose the best parameters. Global methods provides estimates through simultaneously analyzing all FRFs. This yields unique estimates for each mode.

- **Time domain/Frequency domain**
  The FRF data is usually given in the frequency domain. Through use of Fast Fourier Transforms the data can be transformed back to the time domain in which the modal parameters can also be estimated. It has been shown that the frequency domain estimation is less sensitive to noise. This is discussed in Turkay & Ulsoy [14].

A more recent modal parameter estimation method is the *PolyMAX* method. This is a global MDOF frequency domain method. The main advantage of the *PolyMAX* is that it compared to other techniques yields very clear stabilization diagrams and thereby ease of use in identifying the physical modes of the system.

It has also been shown to outperform other methods in terms of computational efficiency[15].

To validate the estimated modal parameters the FRFs of the modal model can be constructed using the estimated modal parameters. This is known as synthesized FRFs. Comparison of the measured FRFs and the synthesized FRFs can be used to verify that the identified modes are physical modes of the system.

As the response is measured at discrete locations of the structure, and thereby may not capture all of the mode shapes, it is of interest to compare the different mode shapes identified. The Modal Assurance Criterion (MAC) between to vectors $\mathbf{\Psi_k}$ and $\mathbf{\Psi_l}$ is defined as:

$$MAC_{k,l} = \frac{|\mathbf{\Psi_k^T \Psi_l}|^2}{(\mathbf{\Psi_k^T \Psi_k})(\mathbf{\Psi_l^T \Psi_l})}. \tag{39}$$

The MAC takes the values: $0 \leq MAC \leq 1$ and defines the correlation between two vectors where 1 indicates identical vectors. In the case of mode shape vectors the MAC can be calculated between experimentally identified mode shapes and mode shapes obtained from e.g. FE-analysis, or between a set of identified mode shapes and itself. In the latter case, a high MAC between two *different* mode shapes can indicate two things. The first being that the response is not measured at enough positions, hence due to the limited resolution of the measurement, two different identified physical modes can appear to have the same mode shape and thereby be correlated. The second that the same mode has been identified twice.

2.6 OMA - Operational modal Analysis

In cases involving difficulty of measuring the input to the system, such as for large structures or structures in operation, EMA can not be applied. This has led to the development of operational modal analysis. The purpose of OMA is to identify the modal parameters of the system under operating conditions, rather than in a lab environment, using only the response measurements. Based on the assumption of white noise input, a modal model is created using only the auto and cross power spectres from measurements. A modal parameter estimation is then performed similar to experimental modal analysis. A thorough introduction to OMA and common modal parameter estimation techniques is given in Brinker[16].

2.7 Pseudo damage

Pseudo damage is calculated to predict the life time of a component based on either simulation or measurement, or to compare measurement and simulation through calculating relative pseudo damage. In fatigue the S-N curve describes the relationship between stress amplitude s and number of cycles to failure N in a log-log diagram, see Figure 3.

Part B of the S-N curve denotes the fatigue limit, below this stress amplitude failure is assumed to not occur for certain materials, e.g. steel in this case. This assumption does not hold for all types of materials. The relationship between stress amplitude and number of cycles to failure for the sloping part A of the curve can be described by Basquin's law:

$$N = Cs^{-\beta} \tag{40}$$

where N is the number of load cycles to failure, s is the stress amplitude and C and β are material constants. A given signal can be divided in to k blocks of

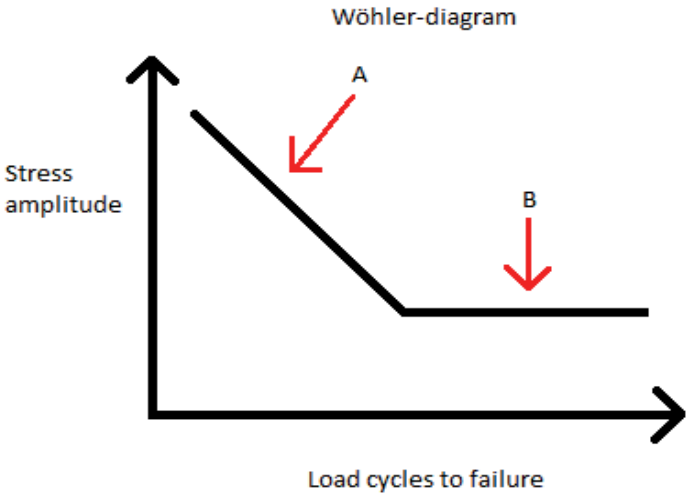

Figure 3: Schematic S-N curve (Wöhler diagram).

different amplitudes, each block containing p cycles using the rainflow algorithm. The idea of the rainflow counting algorithm is for a given signal to count the number of load cycles of a certain amplitude that the signal contains. Doing this for a range of amplitudes the original signal is divided into a number of blocks, each block having a constant amplitude. The number of load cycles at each amplitude being known, Palmgren-Miners linear damage hypothesis can be applied to calculate the pseudo damage for the given signal. The algorithm and its application in fatigue analysis is further described in [17]. The pseudo damage can then be calculated by combining Palmgren-Miners linear damage hypothesis with (40):

$$D = \sum_{i=1}^{k} \frac{p_i}{N_i} = C^{-1} \sum_{i=1}^{k} p_i s_i^{\beta} \tag{41}$$

where N_i is the number of cycles to failure for load i. Failure is set to occur when $D = 1$. The relative pseudo damage is obtained by dividing the pseudo damage D_s for a simulated signal with the pseudo damage for a measured or desired signal D_d.

3 Experimental setup

The experimental setup consists of a part of a chassis frame with a number of components assembled to it including fuel tanks and two different mudguard brackets. The chassis assembly is assembled in the uni-axial test rig called Esso. Using a set of accelerometers mounted at different positions of the setup the structural response is measured for three different excitation signals. An overview of the setup is provided in Figure 4.

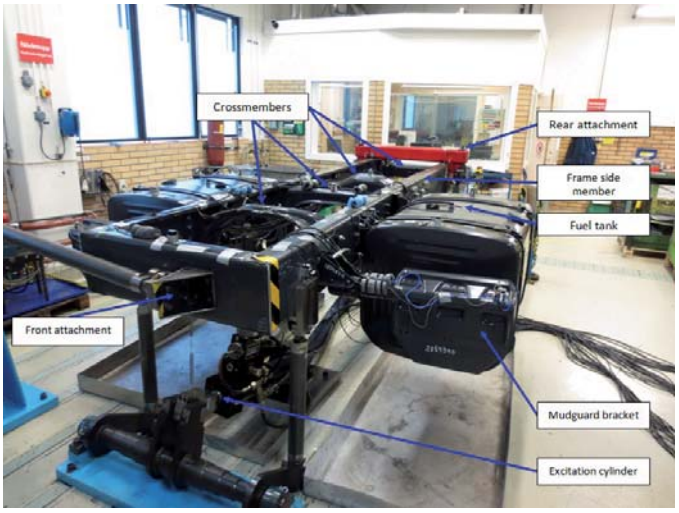

Figure 4: Overview of the experimental setup including a brief description of the components.

3.1 Components used

The main components used in the setup are listed below together with a description:

- **Frame side members**
  The frame side members consists of an outer frame bolted together with an inner frame fitted inside it. The frame side members are made out of sheet steel. In the front end, the side frame side members are welded to a front plate connected to the front attachment of the test rig.

- **Cross members**
  The cross members connects the side frame members. The two front cross members are made of sheet steel and the rear two of cast iron. All of the cross members are connected to the side frame members with bolted joints.

- **Fuel tanks**
  The fuel tanks have a volume of 400 litres and are made of sheet steel. The fuel tanks are filled with 222 liters of water each. They are connected to the frame side members via two brackets bolted to the frame.

- **Mudguard brackets**
  Two different mudguard brackets are used. One of the mudguard brackets is suspended with a rubber bushing. They are connected to the frame side members with bolted joints.

3.2 Excitation system & boundary conditions

The test rig uses a hydraulic cylinder to excite the tested structure in the z-direction. The hydraulic cylinder is connected to the two frame side members through a mechanical linkage. The excitation is controlled by prescribing the displacement of the cylinder. At the front plate, the structure is connected to a strut restraining the motion in the y-direction. At the rear attachment the structure is free to rotate about the y-axis, while it is constrained in the other rotational and translational degrees of freedom. A schematic view of the setup and boundary conditions together with the orientation and origo, denoted by a black dot, of the local coordinate system are given in Figure 5.

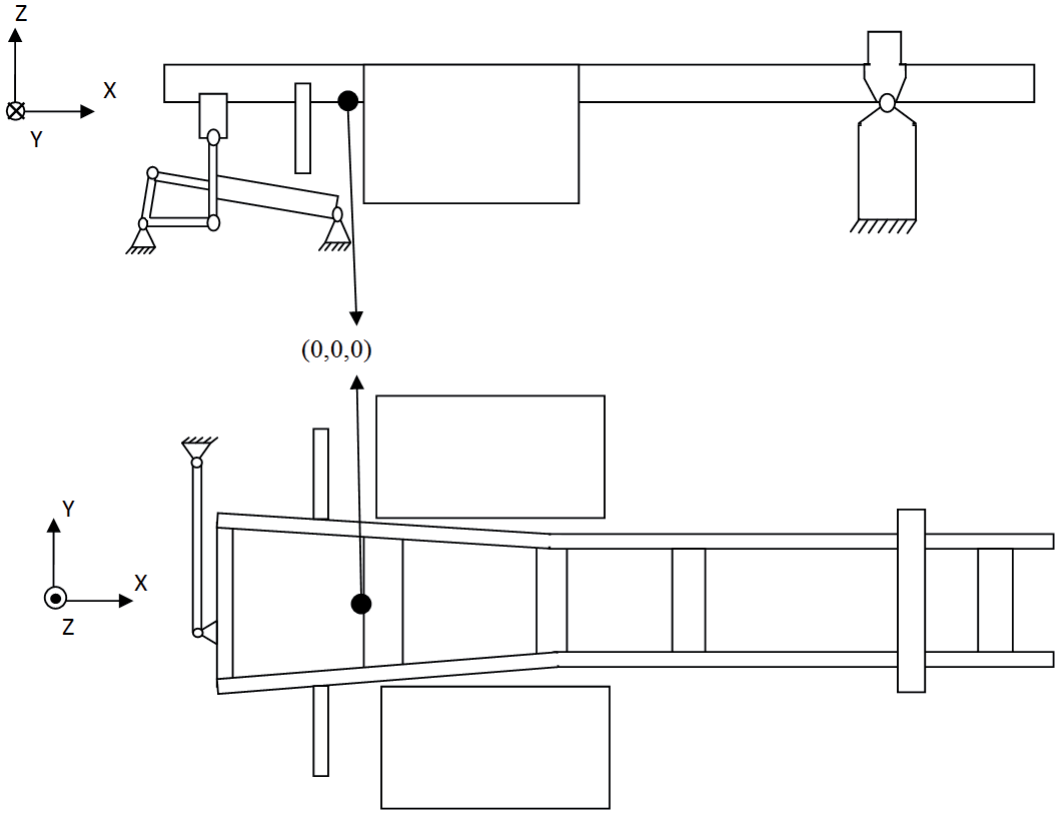

Figure 5: Schematic picture of the setup, showing the mechanical linkage connecting the cylinder to the structure, the boundary conditions and the orientation of the coordinate system

3.3 Sensor arrangement and measurement system

A total of 42 accelerometers were mounted to the chassis assembly of which 21 measured the acceleration response in the z-direction. Since the structure is excited in the z-direction this was considered the response of highest interest. Due to limited availability of accelerometers the response could not be measured in all directions at all of the chosen locations. The response was measured at the positions and directions seen in Figure 6. For each location the measurement directions were chosen based on the anticipated response, i.e. the mudguard brackets were expected to move in all directions, while the frame side members were expected to move mainly in the z-direction. A complete list of the name, position and measurement direction of all used accelerometers is given in Appendix A. Components and accelerometers with a negative y-coordinate will be referred to as on the *left* side and on the *right* side with a positive y-coordinate.

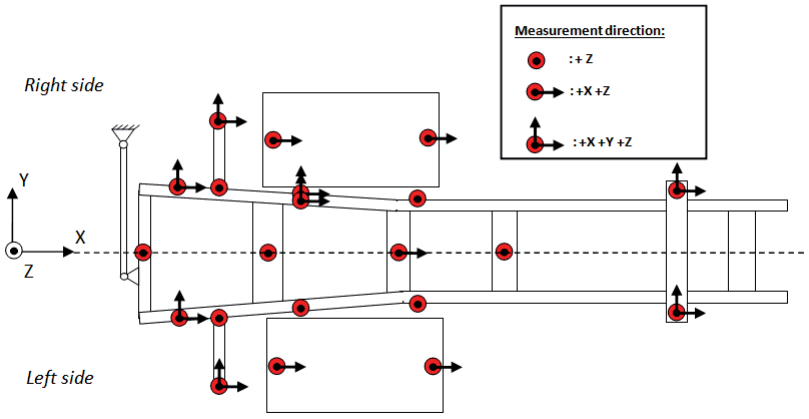

Figure 6: Overview of response measurement locations and directions.

Each accelerometer was attached on to an aluminum cube which was then glued to the structure according to the standard procedure used at Scania, this can be seen in Figure 7. The accelerometers used were specified up to $30g$, g denoting gravitational acceleration. Each accelerometer used had an individual sensitivity, given in Appendix A.

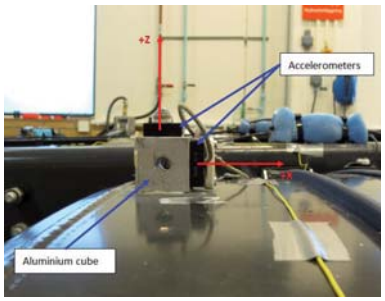

Figure 7: Mounting of accelerometers to the test structure. The red arrows indicates the positive measuring direction for the two accelerometers.

The accelerometers were connected to an external data acquisition system. For each measurement channel the measuring direction was verified, through a manual check. The sensitivity was given for each channel and an acceleration offset applied in the measurement system to remove constant errors in the measurements. The acceleration response was acquired at a sampling rate of 1000 Hz. The displacement of the hydraulic cylinder was measured by the control system of the cylinder and the displacement was acquired at a sampling rate of 204.8 Hz.

4 Modeling the experimental setup

4.1 Modeling procedure

The Multi Body Simulation model of the experimental setup was created in the MBS-software Adams/Car by MSC Software. Three different models of the experimental setup was created, each of the models and their purpose is described in Sections 4.3,4.4 and 4.5. The main difference between the models is how the chassis assembly is modeled, the test rig is identically modeled in all of the models.

The modeling procedure is similar for all three models and consists of three basic steps shown in Figure 8. The first step is to create finite element(FE)-models of the parts that are going to be represented by flexible bodies in the MBS-model, this is done in HyperMesh. For some components FE-models already existed in Scanias library, in this case these models were used and modified to fit, if no model existed it was created based on a CAD-geometry of the part. The rear foundation and rear attachment were modeled based on tape measurements of their dimensions. Secondly the flexible body is generated from the FE-model through a two-step analysis in Abaqus. The first step includes solving the eigenvalue problem and modal truncation. The second Abaqus step includes the Craig-Bampton transformation and orthogonalization of the system to yield the flexible body. The last step consists of MBS-modeling of the rigid parts of the setup and coupling the parts using different joints to restrain the relative motion in selected degrees of freedom between parts. Requests are created in the model, measuring the acceleration response at the same locations as used in the experimental setup. A visualization of the modeling steps is seen in Figure 8.

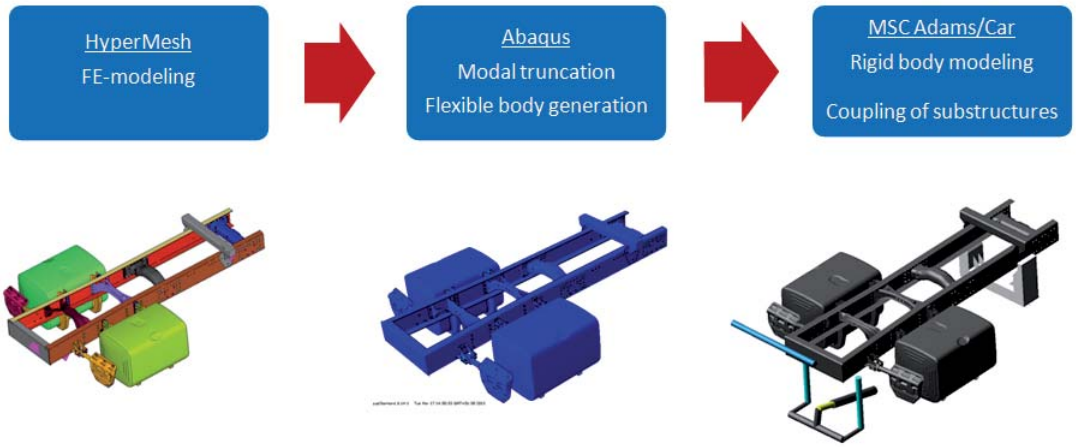

Figure 8: The steps in the modeling procedure, and an overview of the model in each step, note how the excitation system and rear foundation is modeled in the last step.

4.2 Modeling of the test rig

The excitation system and front attachment are modeled as rigid bodies, the dimensions are based on tape measurements of the real test rig. The hydraulic cylinder is connected to the ground through a constant velocity joint, which removes all DOF:s except one rotational DOF, in this case rotation about the y-axis is allowed. A piston (olive green in Figure 9a) is connected to the hydraulic cylinder through a translational joint, allowing translational motion relative to the cylinder in its longitudinal direction. An actuator is used to control the displacement of the piston. The piston is also connected to the mechanical linkage through a spherical joint, removing all translational DOF:s between the two. The mechanical linkage is connected to the ground through two spherical joints, allowing it to rotate about the y-axis, and connected to the two struts through constant velocity joints. The struts (cyan in Figure 9 a) connects the mechanical linkage to the chassis assembly via two spherical joints.

The front attachment is connected to the ground through a constant velocity joint and to the chassis assembly through a spherical joint. The rear foundation is modeled as a flexible body with four interface nodes, two of which connects the foundation to the ground using fixed joints and two connecting it to the chassis assembly using spherical joints. Figure 9 shows the test rig model, which consists of a) the front attachment together with the excitation system and b) the rear foundation.

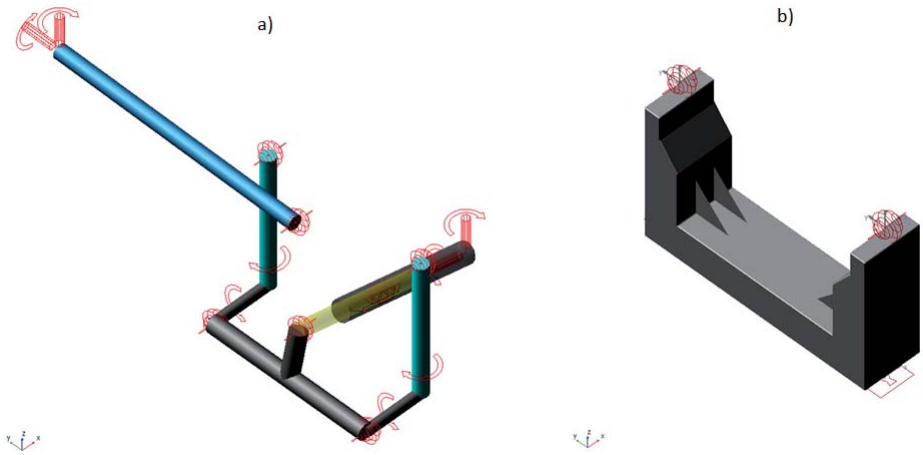

Figure 9: Overview of a) the front attachment and excitation system, including the excitation piston (olive green) and the strut restraining the motion of the structure in the y-direction (blue) and b) the rear foundation.

4.3 Model 1

In Model 1 the chassis assembly is modeled as a single flexible body. Five interface nodes are used to couple the flexible body to the test rig in the MBS-model. In the FE-model the parts are modeled using shell elements with the exception of rubber and cast iron components, for these solid tetrahedral elements are used. To include the mass of the water contained in the fuel tanks in the model, the density of the fuel tank shell elements was increased to account for the mass of the water. In reality the water will move within the fuel tank, hence the centre of gravity of the fuel tank will change with time. This is not taken into account in the model. The average element size varies between 5-10 mm. The different parts are coupled using beam elements as a simplification of what in reality is a bolted joint. This is a simplification that saves time and effort in the modeling process and are currently used in larger models at Scania. Figure 10 shows two different parts connected using a beam element together with kinematic coupling elements as a simplification of the bolt.

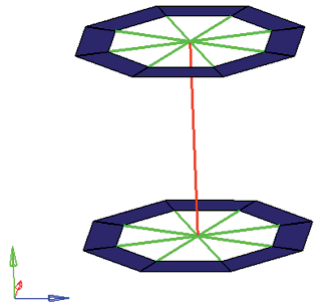

Figure 10: Two parts (blue) connected with a beam element (red) and kinematic coupling elements (green).

The interface nodes are connected to the chassis assembly using kinematic coupling elements. For the generation of the flexible body all the DOF:s of the interface nodes are removed. Modes with associated eigenfrequency above 300 Hz are truncated. This as the excitation signal had a cut-off frequency of 60 Hz, resulting in no or very low excitation of modes with higher frequencies, which are then considered not to affect the dynamic response of the model.

4.4 Model 2

In Model 2 the chassis assembly is also modeled as a single flexible body. Element types and size as well as interface nodes are the same as used in Model 1. In this model however, the different parts are connected using bolts consisting of solid brick elements, together with spacing washers and washers also consisting of solid elements. One of the bolted joints in the FE-model is shown in Figure 11. The purpose of Model 2 is to investigate how modeling of the bolted joints used in Model 1 and 2 respectively affects the dynamic properties of the MBS-model in terms of mode shapes and eigenfrequencies. The detailed modeling of bolted joints in Model 2 is more time consuming compared to Model 1, both with respect to creating the model and computational time.

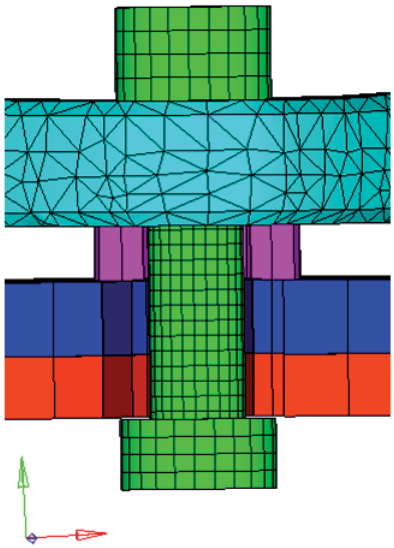

Figure 11: Bolted joint modeled with bolt (green) and washer (purple). Depicted in red and blue are shell elements of frame side members with elements removed to show the bolt, whereas cyan solid elements depicts a part of the right mudguard bracket.

The generation of the flexible body for Model 2 includes finding where contact will occur in the bolted joints in the model as well as applying axial pre-tension to the bolts in the model. Thereafter the model is linearized and the flexible body is generated. As for Model 1 DOF:s of all interface nodes are removed and modes with associated eigenfrequency above 300 Hz are truncated.

4.5 Model 3

In Model 3 the frame side members and cross beams are modeled as one flexible body, while each fuel tank and each mudguard bracket is modeled as separate flexible bodies. The FE-modeling of each flexible body follows the procedure used for Model 1. Two interface nodes are used for each fuel tank and a single interface node for each mudguard bracket, this gives a total of eleven interface nodes for the frame. These separate flexible bodies are connected to each other with fixed joints at each interface node in the MBS-model. MSC Adams/Car provides the possibility of connecting the different parts using force elements to achieve a flexible coupling, due to time limitations the simpler fixed joint was used in this work.

Modeling of components as separate flexible bodies allows for ease of modeling as components can be switched out directly in the MBS-model, not having to create new FE-models. The purpose of Model 3 is to compare how the modeling affects the dynamic properties of MBS-model in terms of eigenfrequencies and mode shapes. The damping is set individually for each of the flexible bodies.

As in Models 1 and 2, in the generation of the flexible bodies the DOF:s of all interface nodes are removed and modes with associated eigenfrequency over 300 Hz are truncated. Figure 12 shows an overview of the complete MBS-model.

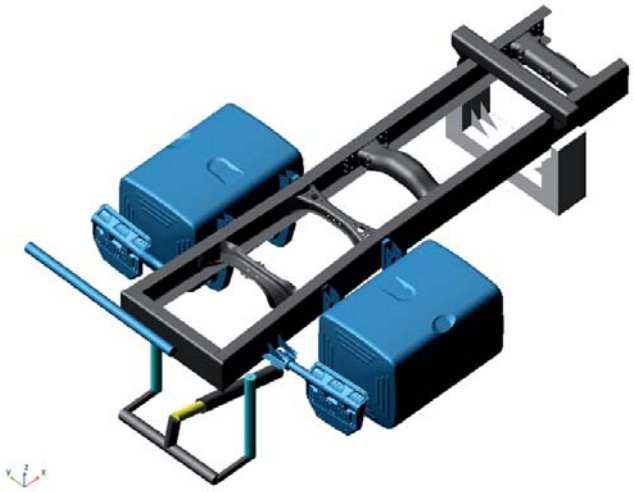

Figure 12: Overview of Model 3.

5 Experimental Modal Analysis

5.1 Identified modal parameters

For the purpose of modal parameter estimation a driving signal was generated. The desired signal is a white noise in the frequency band of 3-60 Hz. Figure 13 shows the displacement power spectral density (PSD) of the desired signal and the signal measured at the hydraulic cylinder. The PSD plot provides an overview of the average squared displacement amplitude as a function of frequency, normalized by the frequency resolution, hence the unit of $[mm^2/Hz]$.

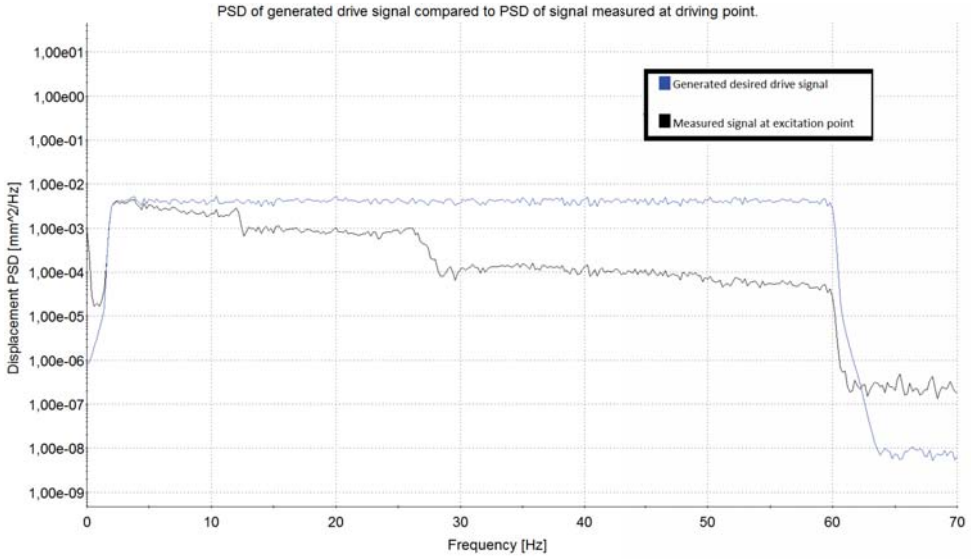

Figure 13: Displacement PSD of desired and measured driving signal. The blue graph shows the desired signal and the black graph the signal measured at the excitation point.

It is observed that the measured driving signal shows two major drop-offs at 12 Hz and and 26 Hz respectively. The result of the drop-offs is a lower excitation amplitude of higher frequencies, compared to the desired flat distribution.

The modal parameter estimation is performed using the commercial software LMS Test.Lab Modal Analysis. The modal parameter estimation method used is the PolyMAX method, recall Section 2.5. Two modal parameter estimations are performed using two different reference accelerometers, *ARFVZ* and *ARFHZ*. These accelerometers are located at the left and right frame side members at the connection between the linkage and the respective frame side member. Frequency response functions were calculated between the references and response channels 1 and 8-42, shown in Table 1 in Appendix A, using the H_v estimator, described in Section 2.5.2, with a frequency resolution of 0.2 Hz.

A total of ten modes are identified in the frequency range 3-50 Hz for both of the used reference accelerometers. Stabilization diagrams are provided in Appendix B. The modal parameters are taken as the average from the two identifications. In Table 1 the natural frequencies and modal damping ratios together with a short mode shape description is provided.

Table 1: Identified modal parameters from white noise signal.

Mode No.	Undamped natural frequency	Modal damping ratio	Mode shape description
1	12.05 Hz	1.81 %	Excitation right fuel tank, z
2	13.21 Hz	1.46 %	Excitation both fuel tanks, z
3	14.15 Hz	1.78 %	Excitation left fuel tank, z
4	15.00 Hz	2.18 %	Excitation left mudguard bracket, z
5	21.21 Hz	1.19 %	Frame bending about z-axis
6	32.69 Hz	5.47 %	Excitation left mudguard bracket x and z
7	36.64 Hz	3.46 %	Excitation left mudguard bracket x and z
8	41.37 Hz	1.19 %	Frame bending about y-axis
9	43.84 Hz	2.09 %	Frame bending about y-axis
10	47.60 Hz	0.53 %	Excitation right mudguard bracket z

The identified modal damping ratio ranges from 0.53% for mode ten in which the right mudguard bracket(without rubber bushing) is excited, to 5.47% for mode six which involves the left rubber suspended mudguard bracket. Overall the damping is higher for modes involving the left mudguard bracket. For modes involving the fuel tanks and frame bending the modal damping ratio ranges from 1.19% to 2.18%. The mode shapes related to excitation of fuel tanks are distinct when visualized. Mode five is the least distinct mode in terms of its mode shape. The mode shapes were visualized in LMS Test.Lab Modal Analysis and the obtained mode shapes are shown in Figure 14, taken as the average of the two parameter identifications. A thread model is created based on the accelerometer locations, each dot in Figure 14 represents a measurement location, these are connected with lines to create a simplified visual representation of the tested structure. Based on the identified mode shape coefficients the mode shapes can then be visualized.

Note in Figure 14 how some mode shapes, e.g. for mode six and ten, are easily distinguished whilst others, e.g mode three and five are harder to distinguish due to the limited measurement locations and directions.

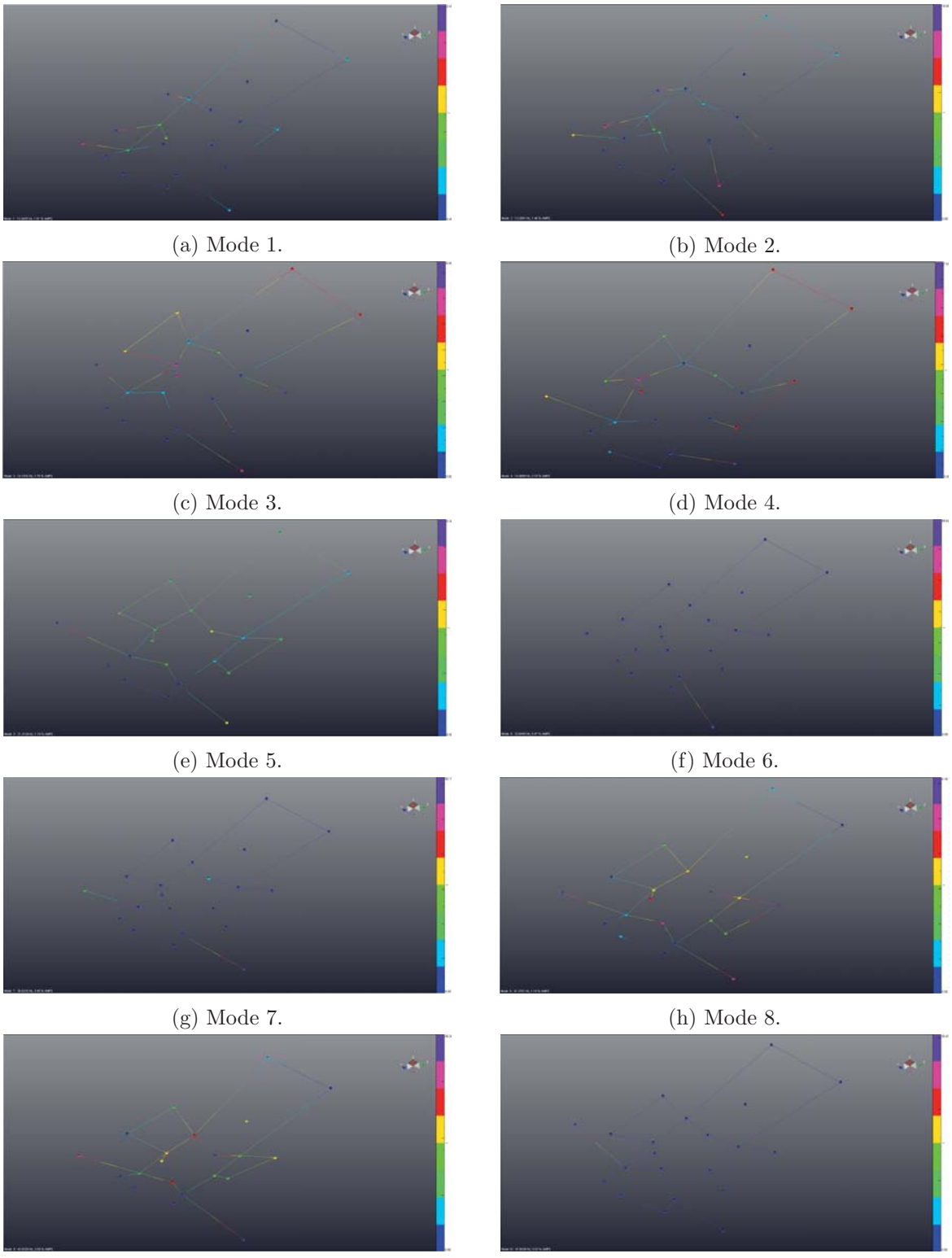

(a) Mode 1.

(b) Mode 2.

(c) Mode 3.

(d) Mode 4.

(e) Mode 5.

(f) Mode 6.

(g) Mode 7.

(h) Mode 8.

(i) Mode 9.

(j) Mode 10.

Figure 14: Identified mode shapes for the experimental setup. The color shows the relative deformation.

The modal assurance criterion (MAC) was calculated between the set of identified modes shown in Table 1 and itself to verify that no modes are identified twice, and to evaluate the correlation between identified mode shapes. The result is plotted in Figure15.

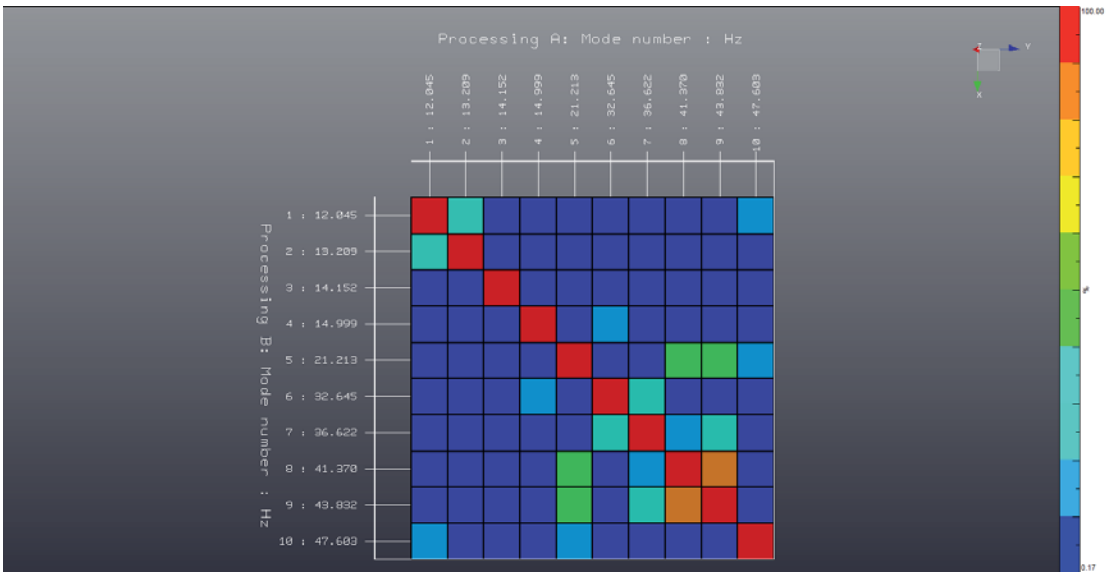

Figure 15: Calulated MAC between a set of identified modes and itself, scale shows correlation in [%] ranging from 0 (blue) to 100 (red).

From Figure 15 it is evident that each mode shows 100% correlation with itself as expected. Overall the correlation between different mode shapes is low with one major exception for mode eight and nine. Studying the corresponding mode shapes both modes shows bending of the frame and can not be distinguished from each other by observation. However they are separated by 2.5 Hz in terms of natural frequency. Mode five shows a correlation of about 50% with respect to mode eight and nine. The mode shape of mode 5 also mainly involves deformation of the frame.

Synthesized frequency response functions were calculated for the two identification procedures, these are presented in Appendix C. The synthesized frequency response functions closely fits the measured ones, especially in the vicinity of the identified natural frequencies.

5.2 Comparison of eigenfrequencies and mode shapes between Experimental Modal Analysis & Multi Body Simulation Models.

To verify that the MBS-models capture the dynamic properties of the experimental setup, they were compared to the identified natural frequencies and mode shapes. For each of the three models the eigenvalue solution for the undamped system was calculated. The identified natural frequencies for each of the models are presented in Table 2, Table 3 and Table 4 together with a brief description of the mode shapes. Visualizations of the calculated mode shapes for each of the models are provided in Appendix D.

Table 2: Calculated natural frequencies together with mode shape descriptions for Model 1.

Mode No.	Undamped natural frequency	Mode shape description
1	11.89 Hz	Excitation left mudguard bracket and fuel tanks, z
2	12.23 Hz	Excitation left mudguard bracket and fuel tanks, z
3	13.21 Hz	Excitation left mudguard bracket, z
4	13.80 Hz	Excitation fuel tanks, z and y
5	20.45 Hz	Frame bending about z-axis
6	32.13 Hz	Excitation fuel tanks and left mudguard bracket, x
7	33.01 Hz	Excitation left mudguard bracket x and z
8	36.35 Hz	Excitation left mudguard bracket, rotation about y-axis
9	47.41 Hz	Excitation right mudguard bracket, rotation about z-axis.
10	51.08 Hz	Frame bending about y-axis

For Model 1 mode shape one to three involves the left mudguard bracket as well as the fuel tanks, in contrary to the experimentally identified mode shapes the mudguard bracket dominates the mode shapes rather than the fuel tanks. Mode six in Model 1 is not found from the experimental modal analysis. Only mode shape ten shows frame bending and its natural frequency is located at 51 Hz compared to the two identified frame bending mode shapes from the experimental modal analysis located at 41 Hz and 44 Hz.

Table 3: Calculated natural frequencies together with mode shape descriptions for Model 2.

Mode No.	Undamped natural frequency	Mode shape description
1	12.03 Hz	Excitation left mudguard bracket and fuel tanks, z
2	13.08 Hz	Excitation left mudguard bracket and fuel tanks, z
3	13.28 Hz	Excitation left mudguard bracket, z
4	14.96 Hz	Excitation fuel tanks, z and y
5	21.11 Hz	Frame bending about z-axis
6	31.54 Hz	Excitation fuel tanks and left mudguard bracket, x
7	32.86 Hz	Excitation left mudguard bracket x and z
8	36.37 Hz	Excitation left mudguard bracket, rotation about y-axis
9	47.63 Hz	Excitation right mudguard bracket, rotation about z-axis.
10	51.13 Hz	Frame bending about y-axis

For Model 2 the calculated modes are the same as for Model 1 with a slight difference in eigenfrequencies. With the exception of mode six and seven the natural frequencies are higher compared to Model 1.

Table 4: Calculated natural frequencies together with mode shape descriptions for Model 3.

Mode No.	Undamped natural frequency	Mode shape description
1	12.12 Hz	Excitation left mudguard bracket and fuel tanks, z
2	13.33 Hz	Excitation left mudguard bracket and fuel tanks, z
3	13.78 Hz	Excitation left mudguard bracket, z
4	16.08 Hz	Excitation fuel tanks, z and y
5	21.45 Hz	Frame bending about z-axis
6	36.39 Hz	Excitation fuel tanks and left mudguard bracket, x
7	36.53 Hz	Excitation left mudguard bracket x and z
8	37.94 Hz	Excitation left mudguard bracket, rotation about y-axis
9	50.07 Hz	Excitation right mudguard bracket, rotation about z-axis.
10	56.17 Hz	Frame bending about y-axis

Studying Table 4 and comparing to Model 1 and Model 2, it is evident that the calculated eigenfrequencies for Model 3 are higher for all modes. For mode six, seven and ten the difference in natural frequency is most notable. Studying the mode shapes of Model 3 it is found that the calculated mode shapes shows similarity with Model 1 and 2.

For each of the identified modes, the calculated mode with the closest matching mode shape was identified for each model. The relative difference in eigenfrequency between the identified modes and the corresponding mode in the model was calculated and is presented in Figure 16.

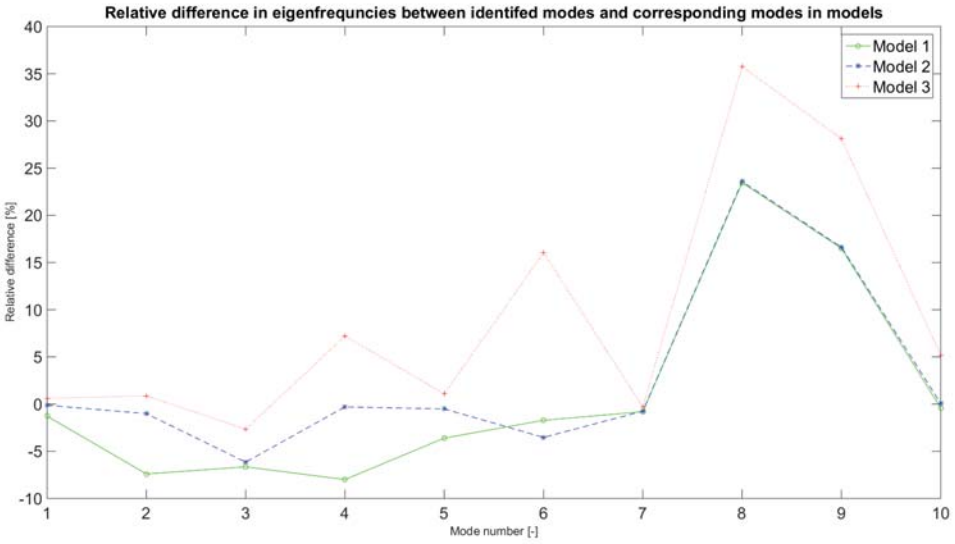

Figure 16: Relative difference in eigenfrequencies between identified modes and corresponding modes in models.

Model 1 shows lower eigenfrequencies for the first five modes and Model 3 shows higher eigenfrequencies except for mode three. For all models the relative difference is largest for the frame bending modes eight and nine, while the eigenfrequency of mode 7 is close to the identified value for all models. Considering the first five modes, for mode one, two, four and five the eigenfrequencies of Model 2 are closest to the identified values.

5.3 Discussion

The first of the two drop offs in the displacement power spectral density for the measured excitation signal in Figure 13 is located close to the first identified eigenfrequency of the system, the second close to an eigenfrequency in the connection between the chassis assembly and the excitation point. The control system of the test rig is not able to compensate for this. As a result the excitation amplitude of the higher frequencies is lower. As the modal damping has been proven to depend on excitation amplitude [5] knowledge of the excitation amplitude is important.

Performing the experimental modal analysis using the PolyMAX method yielded very clear stabilization diagrams and ease of identification. The validation methods used shows good results studying both the modal assurance criterion and the synthesized frequency response functions. Due to the limited number of response measurement directions and locations, interpretation of the mode shapes can prove difficult, in this case especially for the identified mode five. For mode five the frame is deforming, due to the limited number of accelerometers in the y-direction the mode shape is hard to distinguish and compare to the corresponding mode shape in the MBS-models.

For Model 1 the lower frequencies compared to the first five identified modes may indicate that the simplified modeling of bolted joints results underestimates the stiffness, resulting in lower eigenfrequencies. However, for modes seven to ten Model 1 shows almost identical eigenfrequencies compared to Model 2.

Model 2 gives slightly higher calculated eigenfrequencies for modes one to five, indicating that the more detailed modeling of the bolted joints results in a better representation of the actual stiffness.

Coupling the flexible bodies using fixed joints as in Model 3 results in higher frequencies for all modes compared to the other models. Constraining the relative motion in all degrees of freedom at the interfaces between the components shows limitations in representing the dynamic properties of the tested system. To refine the model it would be preferred to connect the flexible bodies using a force element that can represent the stiffness and damping of a bolted joint.

The reason for the big discrepancy between identified modes eight and nine and the corresponding modes of the models has not been identified. All of the models shows a significantly higher eigenfrequency for these modes. A possible source is the modeling method used to include the mass of the water in the fuel tanks. Trying a different modeling approach, e.g. modeling the water as a point mass connected to the fuel tank through distributed coupling elements, and comparing the eigenfrequencies and mode shapes would be of interest. The fact that the motion of the water within the fuel tanks is ignored is also suspected to be a significant source of error.

6 Implementation

6.1 Reference damping functions

Using the identified modal damping presented in Section 5.1, the goal was to find a way of specifying the damping of the flexible bodies in MSC Adams to mimic the identified damping of the physical system. In MSC Adams the modal damping of the flexible body can be specified as an arbitrary function defined by the user, depending on for instance frequency or time. By default the modal damping for mode i of a flexible body is set according to the following:

$$\xi_i = \begin{cases} 1\% & \text{if} \quad 0 < f_i < 100 \quad [\text{Hz}] \\ 10\% & \text{if} \quad 100 < f_i < 1000 \quad [\text{Hz}] \\ 100\% & \text{if} \quad f_i > 1000 \quad [\text{Hz}] \end{cases} \tag{42}$$

where f_i is the natural frequency associated to mode i. The default damping function provided in MSC Adams has proven insufficient because of the low damping of 1 % for modes up to 100 Hz, which are of high interest in heavy vehicle simulations. The currently used damping function was suggested in [18] and uses a step function in MSC Adams for which the modal damping increases with frequency. The Adams step function uses a cubic polynomial to approximate a step function, in this case the transition from 16.6% damping at 0 Hz to 100% at 450 Hz, shown by the blue grpah in Figure 17. The default damping function and the damping function suggested in [18] is plotted below in Figure 17:

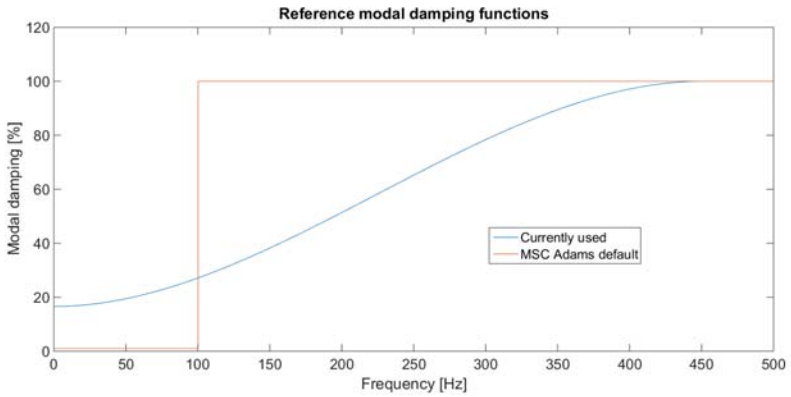

Figure 17: Plot showing two different frequency dependent damping functions used as references.

These two frequency dependent damping functions were used as references in the simulations.

6.2 Suggested damping functions

6.2.1 Model 1 & 2

Recalling the theory in Section 2.4 the flexible body is described by three types of modes, of which one type approximates the modes of the unconstrained flexible body. However, the damping of the physical system is identified under certain boundary conditions, hence the identified modes are not the same as the unconstrained modes of the flexible body, for which the damping is chosen.

The choice of modal damping for the free modes of the flexible body was done through a manual iteration procedure. Based on the modes identified in Section 5.1, the goal was to achieve similar modal damping for the corresponding modes of the complete MBS-models. For Model 1 and 2 this resulted in the modal damping of the free flexible body modes seen below in Figure 18. For higher modes the critical damping was set to 100 %.

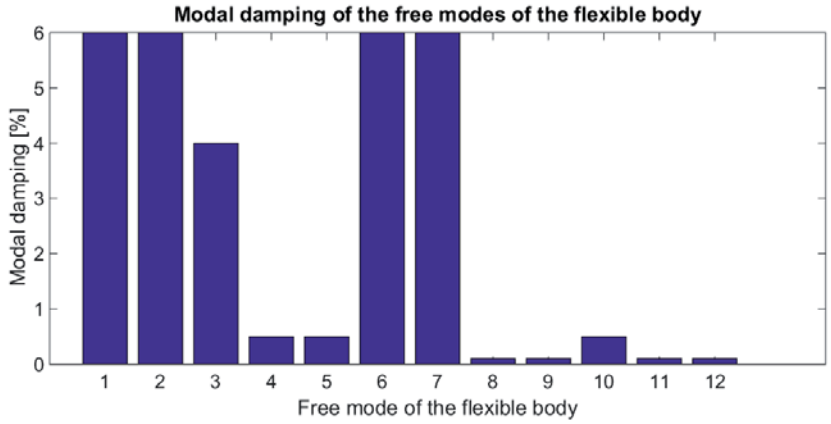

Figure 18: Modal damping of the flexible body.

The chosen modal damping of the flexible body for Model 1 and Model 2, resulted in the modal damping of the complete MBS models presented in Table 5.

Table 5: Modal damping ratios for the modes of the MBS-models 1 and 2, using the suggested damping function.

	Model 1		Model 2	
Mode No.	Undamped natural frequency	Modal damping ratio	Undamped natural frequency	Modal damping ratio
1	11.89 Hz	5.12 %	12.03 Hz	5.84 %
2	12.23 Hz	4.37 %	13.08 Hz	3.68 %
3	13.21 Hz	5.95 %	13.28 Hz	5.97 %
4	13.80 Hz	2.53 %	14.96 Hz	2.79 %
5	20.45 Hz	1.42 %	21.11 Hz	1.48 %
6	32.13 Hz	1.65 %	31.54 Hz	1.51 %
7	33.01 Hz	1.32 %	32.86 Hz	1.90 %
8	36.35 Hz	6.00 %	36.37 Hz	6.00 %
9	47.41 Hz	0.17 %	47.63 Hz	0.18 %

Note that mode 10 is missing compared to Table 2 and Table 3. Using the suggested damping this mode was critically damped and hence did not appear in the results of the damped eigenvalue problem.

6.2.2 Model 3

As Model 3 consists of a number of flexible bodies connected with joints, the damping can be set individually for each of the flexible bodies. For this model the damping was set as a constant value for each of the flexible bodies, the approach used for Model 1 & 2 was deemed too time consuming when dealing with multiple flexible bodies in the model. The chosen values were based on the identified modal damping in Section 5.1. These are presented below in Table 6.

Table 6: Modal damping parameters for the flexible bodies in Model 3.

Flexible body	Frame	Left mudguard bracket	Right mudguard bracket	Left fueltank	Right fueltank
Modal damping	1.5 %	6 %	0.5 %	2 %	2 %

Calculating the damped eigenvalue solution for the complete MBS-model gives the following modal damping seen below in Table 7.

Table 7: Modal damping ratios for the modes of MBS-model 3, using the suggested damping function.

Mode No.	Undamped natural frequency	Modal damping ratio
1	12.12 Hz	0.95 %
2	13.33 Hz	0.96 %
3	13.78 Hz	7.96 %
4	16.08 Hz	4.47 %
5	21.45 Hz	3.16 %
6	36.39 Hz	3.36 %
7	36.53 Hz	16.7 %
8	37.94 Hz	5.33 %
9	50.07 Hz	0.34 %

6.3 Discussion

The differences in mode shapes between the physical system and the models, combined with the fact that the modal damping is chosen for the modes of the flexible body, which differs from those of the physical system, makes the implementation procedure difficult and time consuming.

For Model 1 and 2 the modal damping of the MBS-models is somewhat similar to that of the identified modes. In the four first modes of Model 1 and 2 the left mudguard bracket is more dominant compared to the experimentally identified modes, hence the damping of these modes are chosen higher in the models compared to the identified damping. This is done to better mimic the behaviour of the physical system. To overcome the difficulties in choosing the modal damping of the flexible bodies, it would be preferred to do this using optimization software. Setting the modal damping of the flexible body as design variables and choosing target modal damping of the complete MBS model based on the modal identification procedure to use as goal functions, this would be possible.

For Model 3 the modal damping of the MBS-model using the suggested damping function show little correlation with the identified modes. For many of the modes the frame flexible body is the one mainly deforming. Hence the damping of the modes of the frame would need to be chosen more carefully. To use the modeling procedure of Model 3 it would be preferred to model the bolted joints as force elements in MSC Adams, capturing both stiffness and damping in the bolted joint.

7 Simulation procedures

Using the damping functions suggested in Section 6.2.1 and Section 6.2.2, as well as the reference damping functions, dynamic simulations were performed using three different input signals, which were also used to excite and measure the response of the physical test rig. First the same white noise signal used to identify the modal parameters of the physical system was used. The second signal was a test signal used to represent driving conditions and the third the same test signal with the amplitude scaled down by 50 %. The displacement power spectral density of these three signals measured at the hydraulic cylinder in the physical test is presented in Figure 19 below.

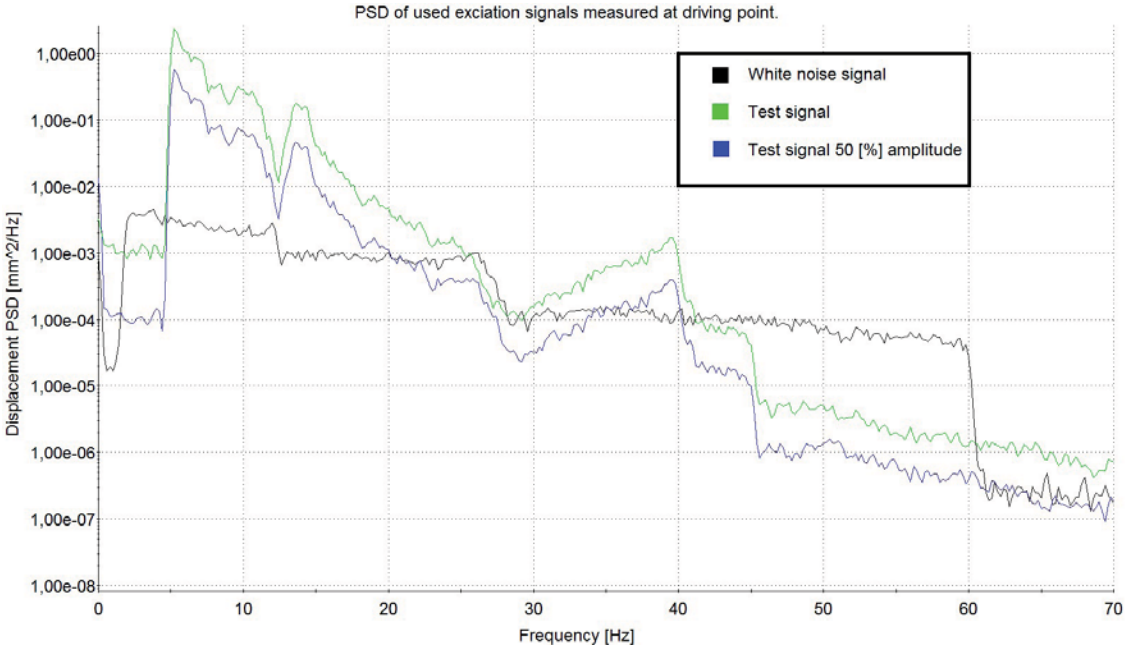

Figure 19: Comparison of the frequency content of the used ecitation signals.

Using the test signals, frequencies between 5-26 Hz and frequencies just below 40 Hz are given a higher excitation.

For each of the simulations the relative pseudo damage, described in Section 2.7, was calculated for accelerometers measuring in the z-direction, using the measured response of the physical system as the desired signal. Recalling equation 40 and 41 in Section 2.7, $\beta = 5$ was used. The choice of β is based on previous experience at Scania, however in general it depends on the material as well as the geometry of the system. For an amplitude difference of $\pm$ 10 % between simulated and desired response, the pseudo damage of the simulated response will range from 59.1-161 % of the pseudo damage of the desired signal.

7.1 Iteration of drive signals

During the first simulations it was discovered that the response at the frame side members, closest to the driving point, differed in amplitude between the simulation and physical measurement, simulation giving a much lower amplitude. Studying the frequency response function between the hydraulic cylinder and the closest response locations on the frame side members in the z-direction, as seen in Figure 20, two clear resonance peaks can be identified around 28 Hz. During the modal identification no mode was found around this frequency, hence the resonance is assumed to be located in the connection between the hydraulic cylinder and the chassis assembly. As the excitation system is modeled using rigid parts this resonance is not captured in the model. The resonance peak just above 12 Hz is due to excitation of the fuel tanks.

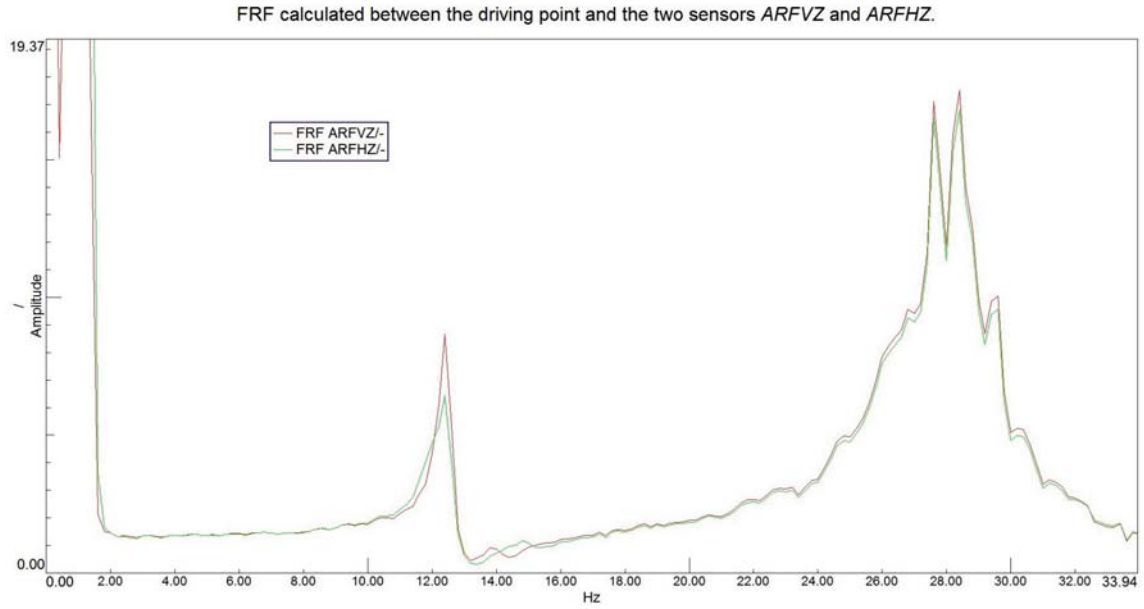

Figure 20: FRF between driving point and closest located sensors on the frame side members in z-direction.

To solve this issue new driving signals were generated for the models using an iteration procedure, where the initial driving signal D_0 is calculated as the measured response A_m multiplied by the inverse of the transfer function H_{AB} between the driving point B and the response A. A simulation is then performed and the error ϵ between simulated and measured response is calculated. The driving signal is then updated by adding the error times the inverse transfer function. This process is repeated until the error is smaller than desired. In this case ten iterations were considered to give a sufficiently small error. The process is described in Figure 21. A more detailed description can be obtained in [19].

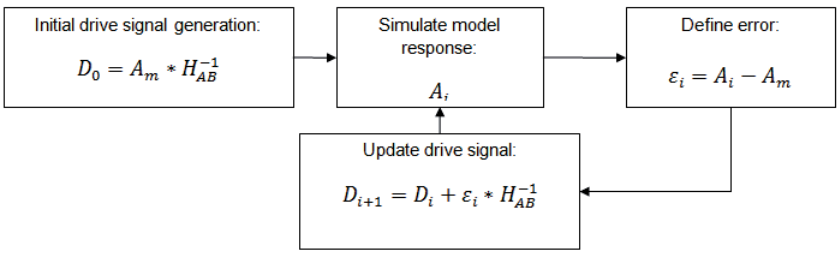

Figure 21: Process for iteration of drive signal.

7.2 Simulations using the white noise signal

Using the white noise the simulation time was set to 80 s using 16384 steps, giving a sampling rate of 204.8 Hz of the simulated response. When calculating the relative pseudo damage, the physical response was resampled from 1000 Hz to 204.8 Hz and the value of β was set to 5.

7.2.1 Model 1

In Figure 22 the simulation results are presented for the suggested damping function and the two references.

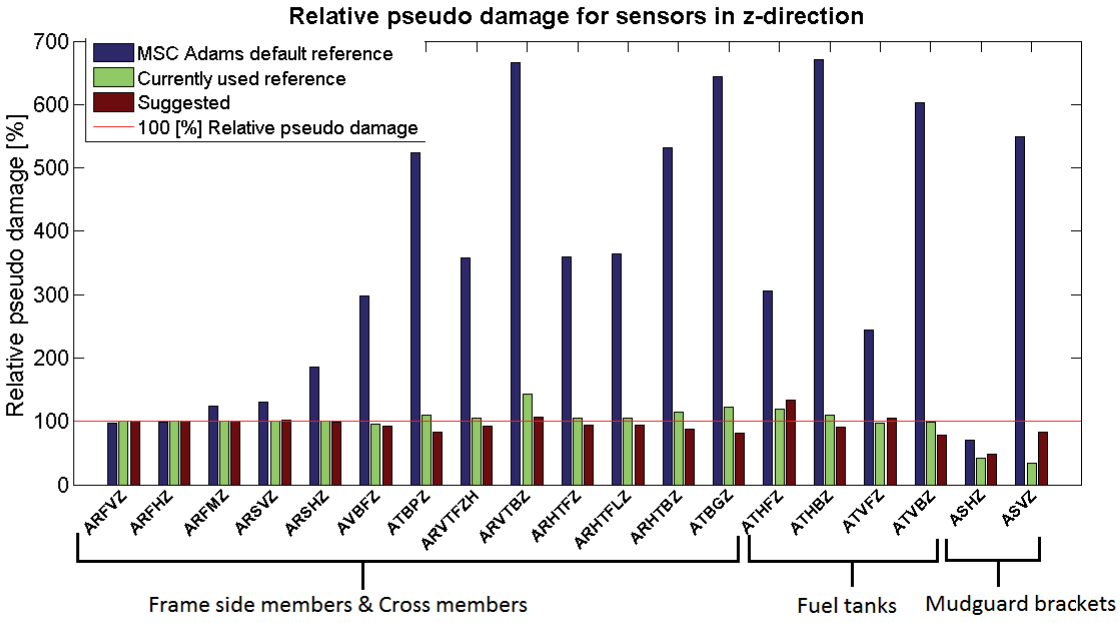

Figure 22: Relative pseudo damage for sensors in the z-direction, using the response from the physical measurement as the desired signal.

The damping does not affect the pseudo damage for the first two sensors *ARFVZ* and *ARFHZ* which is expected as the driving signal is iterated to give the same response for these two locations. Overall the MSC Adams default damping gives an incorrect prediction of the pseudo damage. The currently used damping function and the suggested shows similar predictions with some exceptions. Most notably for the last sensor *ASVZ*, the rubber suspended mudguard bracket, where the suggested damping function gives a better prediction. Also the sensors *ARVTBZ*, which is located at the left frame side member close to the rear mounting of the fuel tank and *ATBGZ* which is the cast iron cross member rear of the fuel tanks. For these the currently used reference damping results in higher prediction of relative pseudo damage compared to Model 1.

7.2.2 Model 2

In Figure 23 the simulation results are presented for the suggested damping function and the two references.

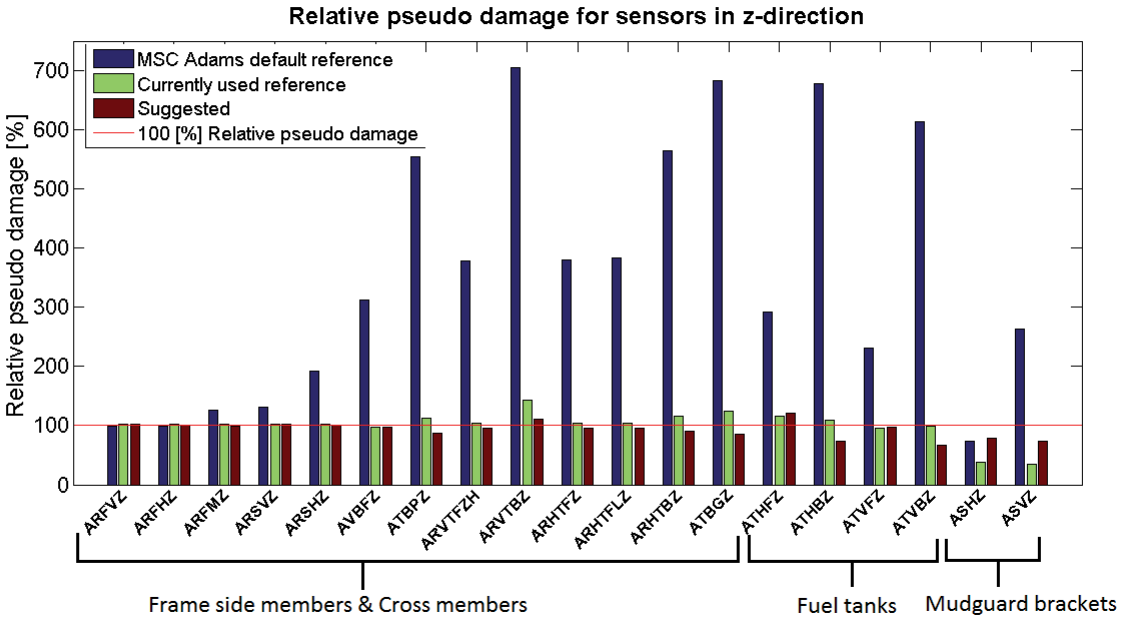

Figure 23: Relative pseudo damage for sensors in the z-direction, using the response from the physical measurement as the desired signal.

For Model 2 similar results are obtained as for Model 1 using the default damping. Once again the currently used damping and the suggested function shows similar results. However Model 2 gives a better prediction of the pseudo damage for both of the mudguard brackets, *ASHZ* and *ASVZ*, using the suggested damping function. It is also noted that sensors mounted to the frame side members and cross members shows similar prediction of pseudo damage for the currently used and suggested damping functions. As in Model 1 the major exceptions are the sensors *ARVTBZ* and *ATBGZ*, however in Model 2 the sensors *ATHBZ* and *ATVBZ* mounted at the rear of the right and left fuel tank respectively, shows a lower predicted pseudo damage using the suggested damping function.

7.2.3 Model 3

In Figure 24 the simulation results are presented for the suggested damping function and the two references.

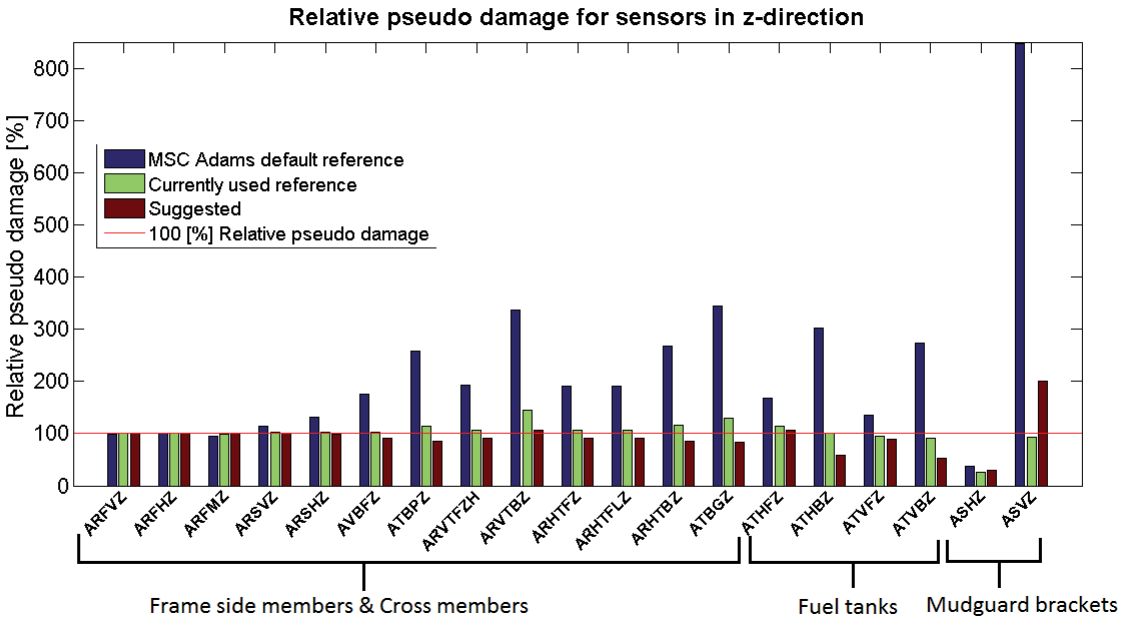

Figure 24: Relative pseudo damage for sensors in the z-direction, using the response from the physical measurement as the desired signal.

Model 3 shows better prediction of the pseudo damage using the default damping function, however for the left mudguard bracket, *ASVZ*, the prediction is very inaccurate. The currently used damping function gives a good prediction of pseudo damage, with the exception of the right mudguard bracket, *ASHZ*, for which all of the used damping functions, the model predicts a lower pseudo damage than what is calculated from measurement. Once again the prediction for sensors *ARVTBZ* and *ATBGZ* shows a higher predicted pseudo damage using the currently used reference damping.

7.3 Simulations using test signals

To further validate the suggested damping functions, simulations were performed using the two test signals. The same simulation time and number of steps were used as in Section 7.2. Again the relative pseudo damage between simulated response and physical measurements was calculated for sensors measuring acceleration response in the z-direction in the same manner as in Section 7.2

7.3.1 Model 1

In Figure 25 the simulation results are presented for the suggested damping function, using the three different signals in Model 1.

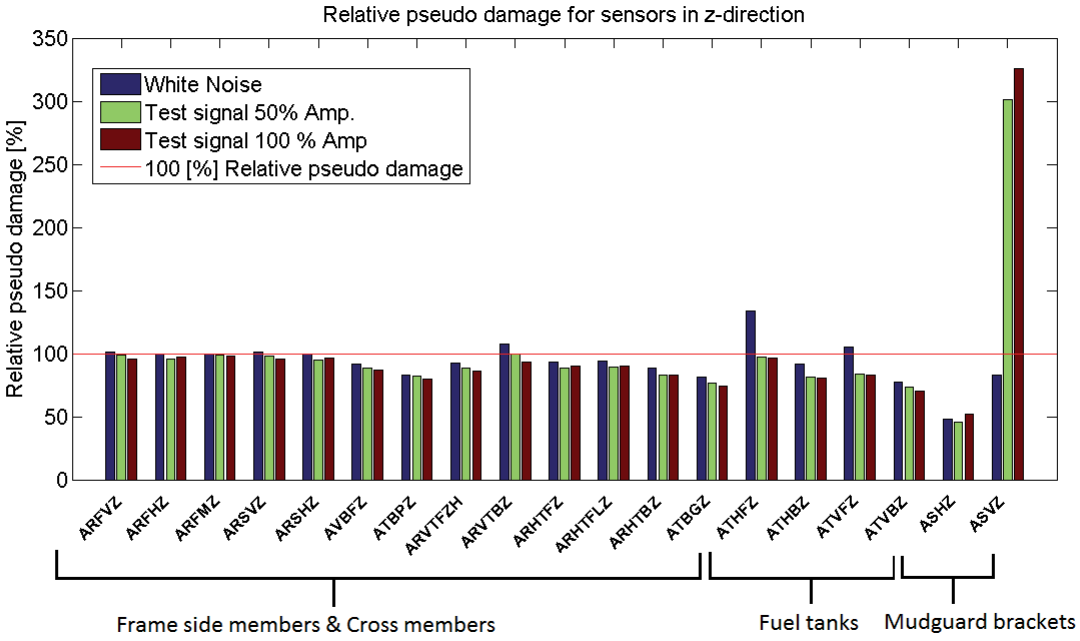

Figure 25: Relative pseudo damage for sensors in the z-direction, using the response from the physical measurement as the desired signal.

Senors located on the frame side members and cross members show marginal differences to change in the excitation signal. The front sensors on both of the fuel tanks, *ATVFZ* & *ATHFZ*, shows a decrease in relative pseudo damage using the test signals compared to the white noise signal. As for the left rubber suspended mudguard bracket *ASVZ*, the relative pseudo damage increases more than threefold using any of the two test signals.

7.3.2 Model 2

In Figure 26 the simulation results are presented for the suggested damping function, using the three different signals in Model 2.

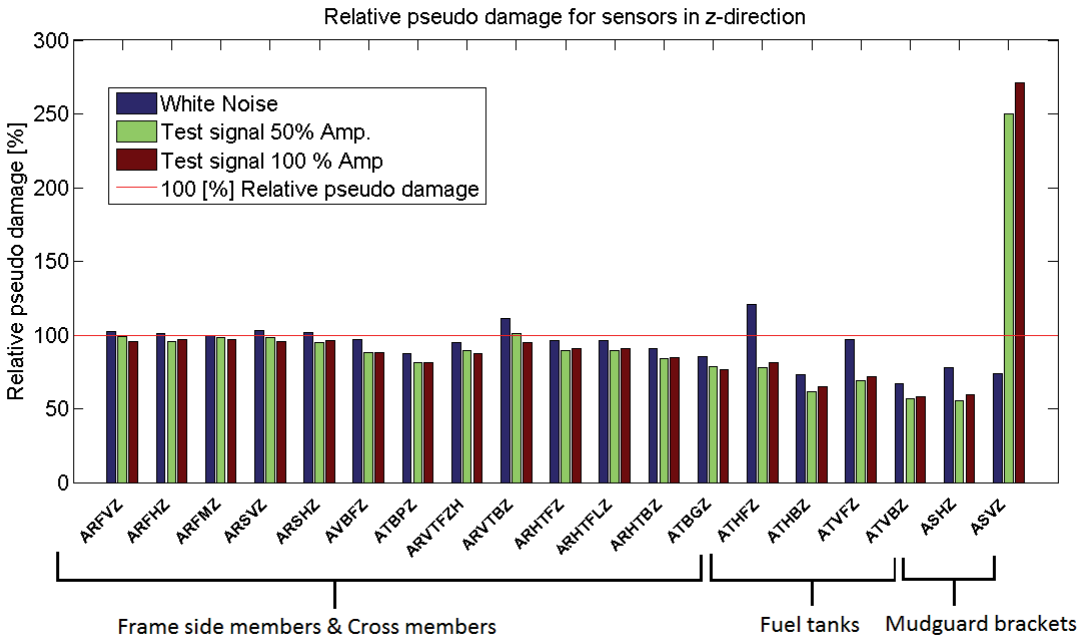

Figure 26: Relative pseudo damage for sensors in the z-direction, using the response from the physical measurement as the desired signal.

Model 2 shows very similar behaviour compared to Model 1 when studying the calculated relative pseudo damage. Note that for the right mudguard bracket *ASHZ*, the relative pseudo damage decreases using the test signals, more so than in Model 1.

7.3.3 Model 3

In Figure 27 the simulation results are presented for the suggested damping function, using the three different signals in Model 3.

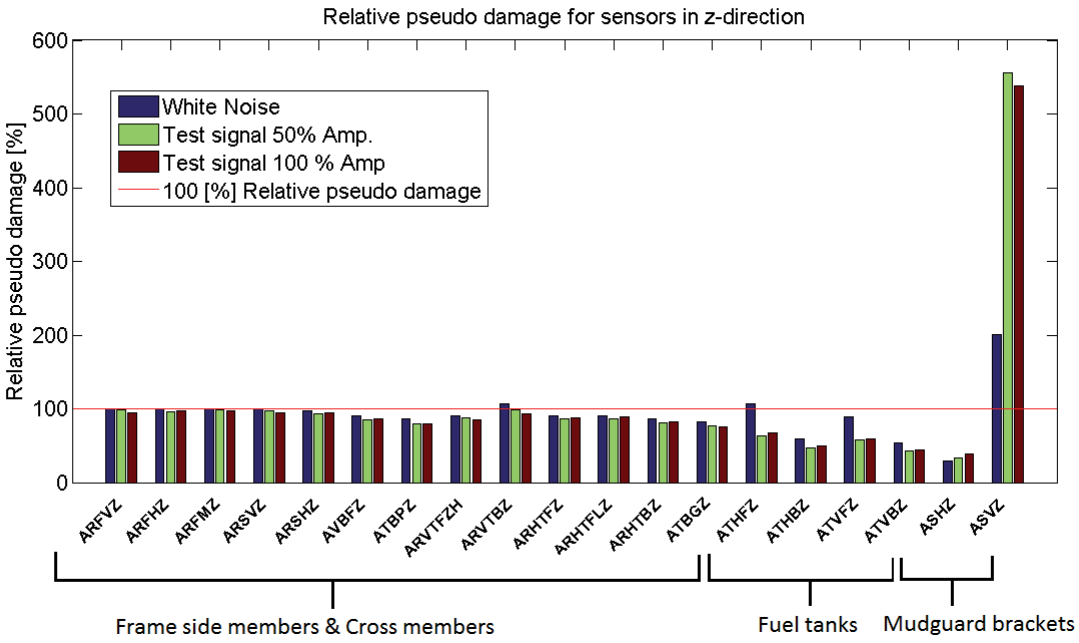

Figure 27: Relative pseudo damage for sensors in the z-direction, using the response from the physical measurement as the desired signal.

For Model 3 sensors mounted to frame side members and cross beams show marginal differences to change in the excitation signal, similar to Model 1 and 2. The front fuel tank sensors $AVTFZ$ and $AHTFZ$, also shows a decrease in relative pseudo damage when using the test signals compared to the white noise. For the rubber suspended left mudguard bracket $ASVZ$, the increase in pseudo damage is close to three fold comparing the test signals to the white noise signal.

7.4 Discussion

Modeling of the excitation system using rigid parts proved insufficient to capture local resonances in this part of the test rig. As the source of the resonance is unknown and hard to locate, correct modeling of this part of the test rig is deemed difficult. The problem is overcome by iterating new drive signals, which gives similar response at the connection between the excitation system and chassis assembly.

Studying how well the different damping functions performs when predicting the pseudo damage through simulation, it is evident that the default damping of flexible bodies in MSC Adams does not perform well, the low damping gives high acceleration amplitudes and thereby a high pseudo damage, compared to responses measured in the physical system.

Comparing the suggested damping function and the currently used reference damping function, it can be seen that for sensor locations on the frame side members and cross members the predicted pseudo damage is not affected by damping. This seems logical as the main source of damping is energy losses due to motion in bolted joints. For the fuel tanks and the mudguard brackets the choice of damping is more important as model input to correctly predict the pseudo damage.

As the excitation signal is changed, sensors located at frame side members and cross members once again shows marginal differences in predicted pseudo damage compared to using the white noise signal. When comparing the currently used reference and the suggested damping functions, the sensors located on the fuel tanks and the mudguard brackets are sensitive to changes in the input signal. As the damping is assumed to depend on excitation amplitude and these sensors being mostly affected by the choice of damping, it seems reasonable that these sensors would be more affected comparing the relative pseudo damage. Knowledge of amplitude differences between the signal used for identification and the signal used for simulation is therefore important.

The left rubber suspended mudguard bracket shows the biggest discrepancy in relative pseudo damage for different excitation signals. The flexible body is a linear model. This means that a linear elastic material model is used to describe the rubber stiffness. Further the deformation of the flexible body relative its own frame of reference is assumed to be small. In the MBS-models mode shapes one to four includes deformation of the left mudguard bracket. Using the test signals the excitation of modes one to four is more powerful compared to the white noise signal. Given these circumstances the extreme increase in relative pseudo damage for the left mudguard bracket observed when using the test signals can be explained by large deformations in the rubber component, violating the assumptions of the linear model stated above. This could be solved by modeling the mudguard bracket as a separate flexible body connected to the frame with a more advanced coupling element.

8 Conclusion

It is concluded that the modal identification procedure performed using LMS Test.Lab Modal Analysis and the PolyMAX method proved to be efficient and easy to use, especially because of the clear stabilization diagrams obtained from the PolyMax method. The used method is powerful for comparing modal properties of models with the modal properties of physical systems, both in FE-simulation and MBS.

Comparing Model 1 and 2, we can conclude that the different methods used for modeling the bolted joints results in minor differences in the modal properties for the first six modes of the models and for mode seven to ten the modal properties are close to identical. As the simplified modeling of the bolted joints used in Model 1 provides more efficient modeling this method is recommended.

Model 3 is advantageous in the sense that modeling of the components as separate flexible bodies provides for easier modification of the model, e.g. if there is need to switch out certain components as the fuel tanks, then only the flexible bodies of the fuel tanks need to be replaced, not having to replace or generate new flexible bodies for the other parts of the setup. However the simplified coupling of the flexible bodies used in this work leaves room for improvement. It is suggested that a method for coupling the flexible bodies using force elements in MSC Adams is developed.

The suggested implementation is associated with difficulties and requires knowledge about the modal properties of the MBS-model as well as the physical system. The method of applying a unique modal damping for the modes of the flexible body provides better ability to predict the pseudo damage on components attached to the chassis frame, such as mudguard brackets and fuel tanks. The method needs to be improved for easier usage, e.g. by using optimization software to select the damping of the flexible body modes.

From the performed simulations it is confirmed that if the signal used in the simulation differs in frequency content from the signal used for identifying the modal damping, the ability to predict the pseudo damage is affected. It also noted that when dealing with parts made of e.g. rubber that may exhibit nonlinear material properties or large deformations in the simulation, care has to be taken as the flexible body in MSC Adams is a linear model.

Finally it can be concluded that the objectives stated in Section 1.2 are achieved. However further investigations are suggested to create more robust methods of implementing identified damping in MBS-models.

9 Future work

In the conducted work two main points are identified as of interest for further investigation, these are presented below:

- Improve the implementation suggested for Model 1 and 2 by using optimization software in combination with MSC Adams simulations. It is suggested that the modal damping of each of the modes of the flexible body are used as design variables. The desired modal damping of the modes of the complete MBS-model can be set based on a modal identification procedure of the physical system.

- Create a force element in MSC Adams which accurately represents the stiffness and damping properties of a bolted joint. If the stiffness and damping properties can be correctly modeled in MSC Adams the problems related to selecting the modal damping of the flexible bodies can be overcome. This would allow for improvement of the modeling procedure used for Model 3.

10 References

References

[1] Bert C.W., *Material damping. An introductory review of mathematic measures and experimental technique*, Journal of Sound and Vibration, 29(2), 1973. DOI: 10.1016/S0022-460X(73)80131-2. Retrieved: 13th of April 2015.

[2] Beards C.F, *Structural Vibration Analysis: Modelling, Analysis, and Damping of Vibrating Structures*, Halsted Press, ISBN: 978-0-340-64580-2, 1983. Retrieved: 13th of April 2015.

[3] Gaul L., *Tutorial Guideline VDI 3830: Damping of Materials and Members* Topics in Modal Analysis 1, Volume 5, Proceedings of the 30th IMAC, A Conference on Structural Dynamics, DOI 10.1007/978-1-4419-9299-4_2 2012. Retrieved: 13th of April 2015.

[4] Xu W., Hess D. P., *Effect of Fastener Preload on Structural Damping*, Journal of Failure Analysis and Prevention, 13, DOI: 10.1007/s11668-013-9740-z 2013. Retrieved: 14th of April 2015.

[5] Wentzel H., *En metod för skattning av dämpning orsakad av skruvförband.*, Technical report, Scania internal documentation 2004.

[6] Hudson D. E., *Equivalent Viscous Friction for Hysteric Systems with Earthquake-Like Excitations*, Proc. 3rd WCEE, New Zealand, Retrieved from: `http://www.iitk.ac.in/nicee/wcee/article/vol2_II-185.pdf` 1965. Retrieved: 13th of April 2015.

[7] He J., Fu Z-F., *Modal Analysis*, Oxford,Boston, Butterworth-Heineman, ISBN: 9780080511788, 2001.

[8] Rayleigh J. W. S., *The theory of sound*, London, Macmillan and co. 1877. ISBN: 978-1-108-03220-9

[9] Unknown athour., *Theory of Flexible Bodies*, MSC Adams 2014 Online Help, 2014.

[10] Wijker J. J., *Spacecraft Structures*, Berlin, Springer, 2008. ISBN: 978-3-540-75553-1.

[11] Verboven P., *FREQUENCY-DOMAIN SYSTEM IDENTIFICATION FOR MODAL ANALYSIS*, Phd Thesis, VRIJE UNIVERSITEIT BRUSSEL, 2002. Retrieved from: `http://mech.vub.ac.be/avrg/PhD/thesis_PV_web.pdf` on the 8th of April 2015.

[12] Beliveau J. -G., Vigneron F. R., Soucy Y., Draisey S., *MODAL PARAMETER ESTIMATION FROM BASE EXCITATION*, Journal of Sound and Vibration, 107(3), ISBN: 1461424259 1986.

[13] Bergström H., *METOD FÖR MODALANALYS AV CHASSIMONTERADE KOMPONENTER I SKAKRIGG*, Technical report, Scania internal documentation, 2002.

[14] Turkay O., Ulsoy A. G., *FREQUENCY VERSUS TIME DOMAIN PARAMETER ESTIMATION: APPLICATION TO A SLOT MILLING OPERATION*, Mechanical Systems and Signal Processing, 2(3), 1988. DOI: 10.1016/0888-3270(88)90023-4. Retrieved on the 8th of April 2015.

[15] Peeters B., Lowet G., Van der Auweraer H., Leuridan J., *A New Procedure for Modal Parameter Estimation*, Sound and Vibration, January, 2004. Retrieved from: `www.sandv.com/downloads/0401peet.pdf` on the 17th of April 2015.

[16] Brinker R., *Some Elements of Operational Modal Analysis*, Shock and Vibration, Volume 2014. DOI: 10.1155/2014/325839. Retrieved: 17th of April 2017.

[17] Baek S. H., Cho S. S., Joo W. S., *FATIGUE LIFE PREDICTION BASED ON THE RAINFLOW CYCLE COUNTING METHOD FOR THE END BEAM OF A FREIGHT CAR BOGIE*, International Journal of Automotive Technology, Vol. 9, 2008, DOI:10.1007/s12239-008-0012-y. Retrieved: 23rd of June 2015.

[18] Sjödin F., *Datorsimulering av skakrigg med F700 ram*, Technical report, Scania internal documentation, 2007.

[19] Bladh K., *Virtual full vehicle durability testing of a coach*, Master Thesis, KTH Stockholm, Scania internal documentation, 2012.

11 Appendix

11.1 Appendix A

Number, name, sensitivity, measurement direction, description and position of used accelerometers. The coordinates are given in mm in a local coordinate system which relates to the standard global truck coordinate system used at Scania according to:

$$\begin{aligned} X_{global} &= X_{local} + 3200 \\ Y_{global} &= Y_{local} \\ Z_{global} &= Z_{local} + 1000 \end{aligned}$$

Table 8: Table describing used accelerometers and their positioning.

					Position [mm]		
Number	Name	Sensitivity [(mV)/(m/sˆ2)]	Positive direction	Description	X	Y	Z
1	ARFMZ	6,741	Z	Frame front center	-530	-5	315
2	ARFVX	6,804	X	Frame front left attachment	-300	-455	170
3	ARFVY	6,873	Y	Frame front left attachment	-315	-475	170
4	ARFVZ	6,764	Z	Frame front left attachment	-315	-455	190
5	ARFHX	6,337	X	Frame front right attachment	-300	455	150
6	ARFHY	6,584	Y	Frame front right attachment	-315	475	150
7	ARFHZ	6,509	Z	Frame front right attachment	-315	455	170
8	AVBFZ	6,411	Z	First crossmember center	125	0	270
9	ARVTFZ	6,716	Z	Frame left front fuel tank	450	-425	245
10	ARVTBZ	6,215	Z	Frame left rear fuel tank	935	-400	245
11	ARHTFXH	6,496	X	Frame right front fuel tank high	465	420	215
12	ARHTFYH	6,224	Y	Frame right front fuel tank high	445	440	215
13	ARHTFZH	6,453	Z	Frame right front fuel tank high	445	420	235
14	ARHTFXL	6,319	X	Frame right front fuel tank low	475	420	55
15	ARHTFYL	6,152	Y	Frame right front fuel tank low	455	440	55
16	ARHTFZL	6,841	Z	Frame right front fuel tank low	455	420	75
17	ARHTBZ	6,839	Z	Frame right rear fuel tank	955	395	240
18	ATBGZ	6,851	Z	Third crossmember center	1475	-10	300
19	ARVBX	6,855	X	Rear attachment left	2490	-535	210
20	ARVBY	6,659	Y	Rear attachment left	2470	-555	210
21	ARVBZ	6,252	Z	Rear attachment left	2470	-535	230
22	ARHBX	6,697	X	Rear attachment right	2500	535	210
23	ARHBY	6,312	Y	Rear attachment right	2480	555	210
24	ARHBZ	6,625	Z	Rear attachment right	2480	535	230
25	ATBPX	6,381	X	Second crossmember center	855	0	260
26	ATBPZ	6,453	Z	Second crossmember center	875	0	280
27	ATHFX	6,45	X	Right fuel tank front	225	835	285
28	ATHBX	6,23	X	Right fuel tank rear	1030	835	285
29	ATHBZ	6,336	Z	Right fuel tank rear	1050	835	305
30	ATVBX	6,288	X	Left fuel tank rear	1050	-825	285
31	ATVBZ	6,247	Z	Left fuel tank rear	1070	-825	305
32	ATVFX	6,247	X	Left fuel tank front	250	-815	285
33	ARSVZ	6,522	Z	Frame left mudguard bracket	-150	-450	230
34	ASHX	6,326	X	Right mudguard bracket	-115	1155	95
35	ASHY	6,764	Y	Right mudguard bracket	-95	1175	95
36	ASHZ	6,608	Z	Right mudguard bracket	-95	1155	115
37	ASVX	6,596	X	Left mudguard bracket	-130	-1148	105
38	ASVY	6,543	Y	Left mudguard bracket	-110	-1128	105
39	ASVZ	6,293	Z	Left mudguard bracket	-110	-1148	125
40	ATVFZ	6,564	Z	Left fuel tank front	230	-815	305
41	ATHFZ	6,951	Z	Right fuel tank front	205	835	305
42	ARSHZ	6,465	Z	Frame right mudguard bracket	0	435	130

11.2 Appendix B

Identified modal parameters stabilization diagrams and synthesized FRFs are shown for the modal identification using *ARFVZ* and *ARFHZ* as references respectively.

11.2.1 ARFVZ

In Table 9 the modal parameters are shown. Figure 28 shows the obtained stabilization diagram. Figure 29, 30 and 31 shows amplitude plots of the of the measured(red) and synthesized(green) FRFs.

Table 9: Identified modal parameters using *ARFVZ* as reference.

Mode No.	Undamped natural frequency	Modal damping ratio	Mode shape description
1	11.99 Hz	2.04 %	Excitation right fuel tank, z
2	13.17 Hz	1.58 %	Excitation both fuel tanks, z
3	14.31 Hz	1.70 %	Excitation left fuel tank, z
4	14.90 Hz	2.28 %	Excitation left fuel tank, z
5	21.21 Hz	1.15 %	Frame bending about z-axis
6	32.77 Hz	5.30 %	Excitation left mudguard bracket x and z
7	36.76 Hz	3.65 %	Excitation left mudguard bracket x and z
8	41.62 Hz	0.79 %	Frame bending about y-axis
9	43.17 Hz	2.09 %	Frame bending about y-axis
10	47.78 Hz	0.483292 %	Excitation right mudguard bracket z

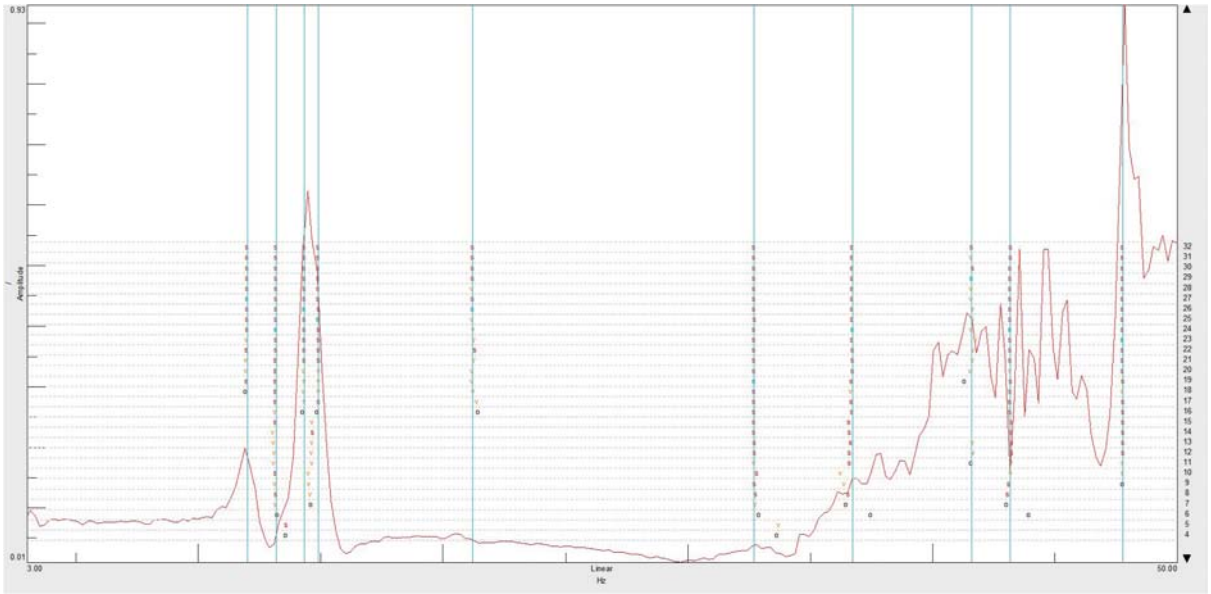

Figure 28: Stabilization diagram. The red curves shows the sum of used FRFs, model size N is indicated on the right hand side, s denotes stable reoccurring modes.

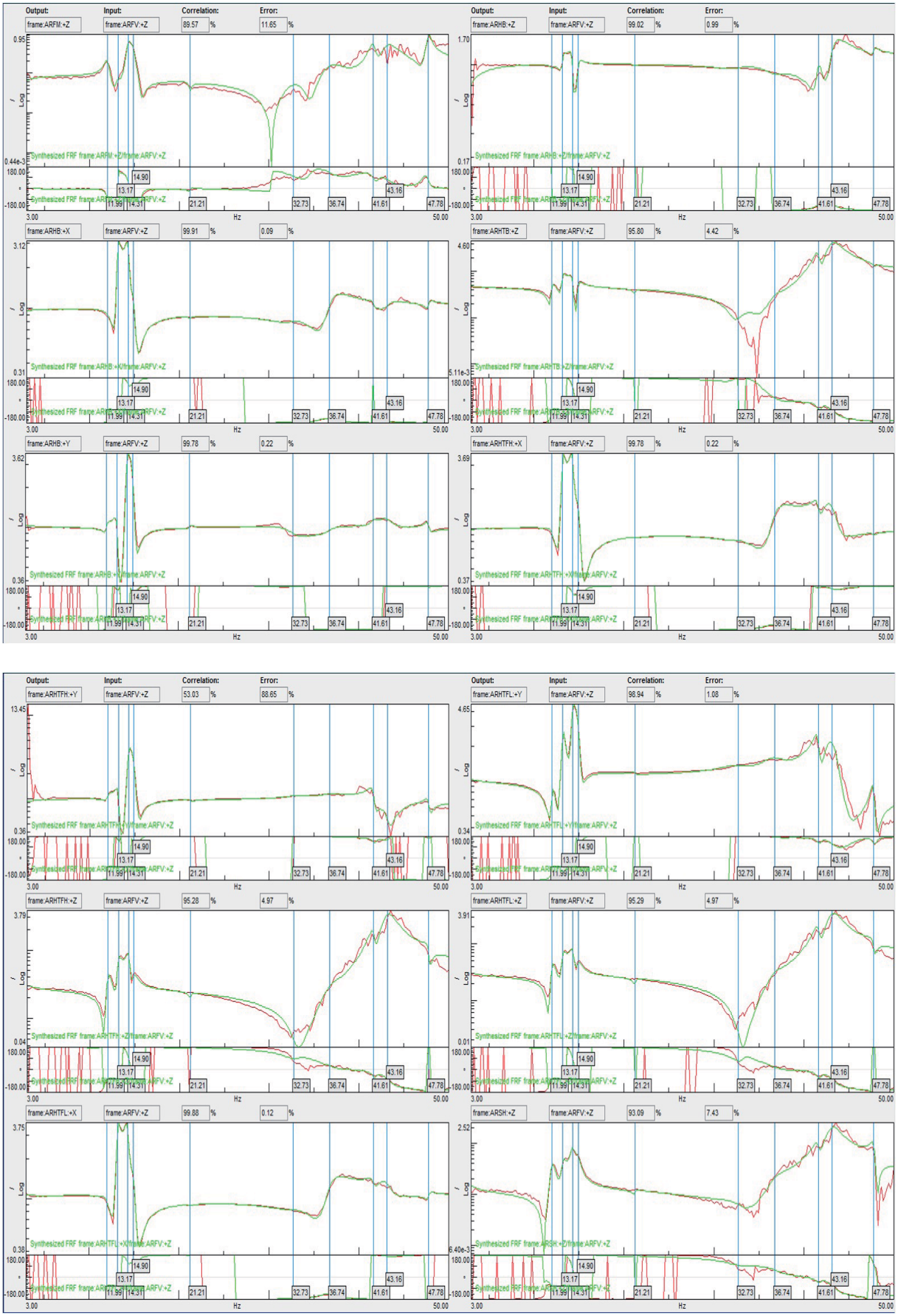

Figure 29: Synthesized FRFs.

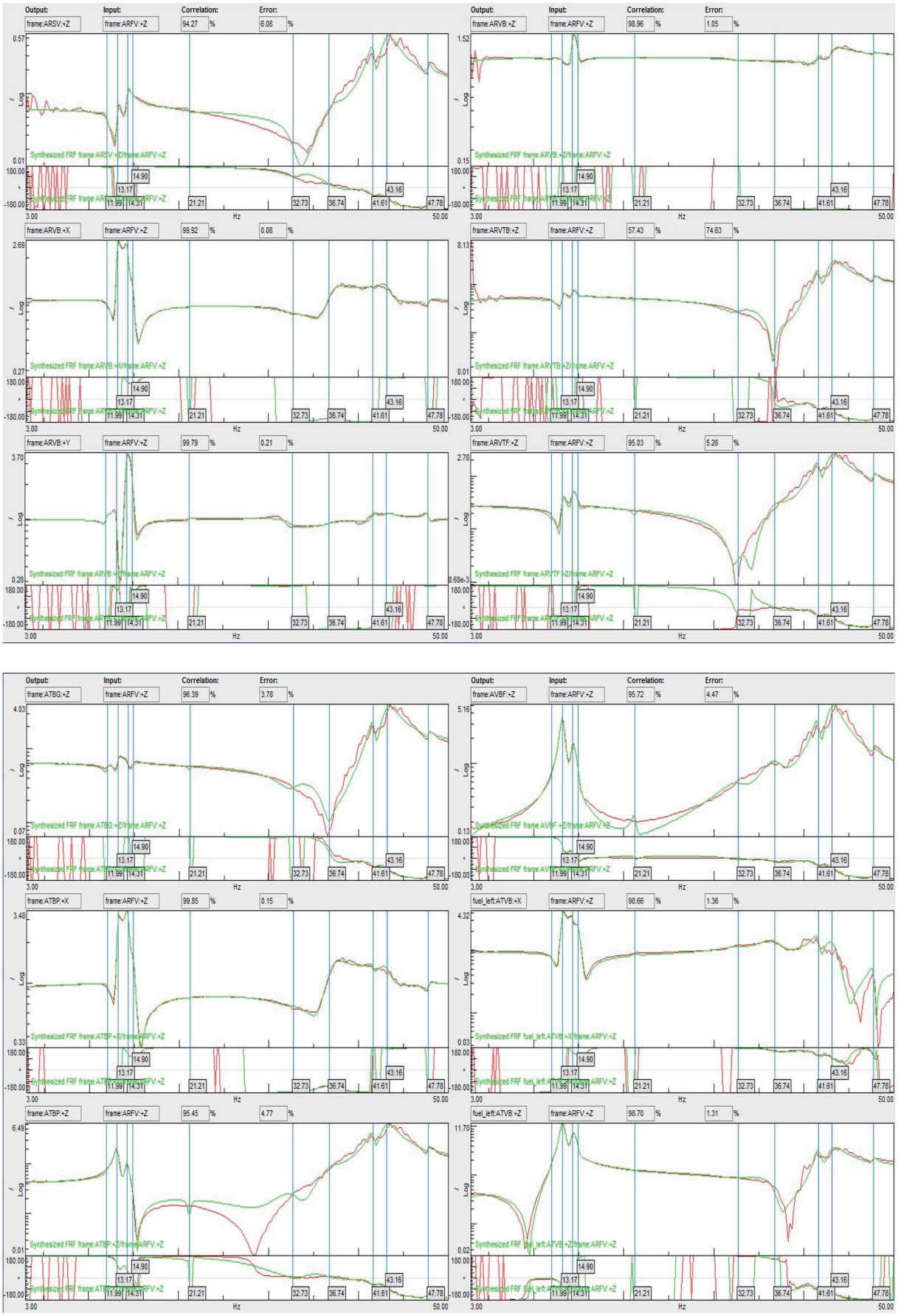

Figure 30: Synthesized FRFs

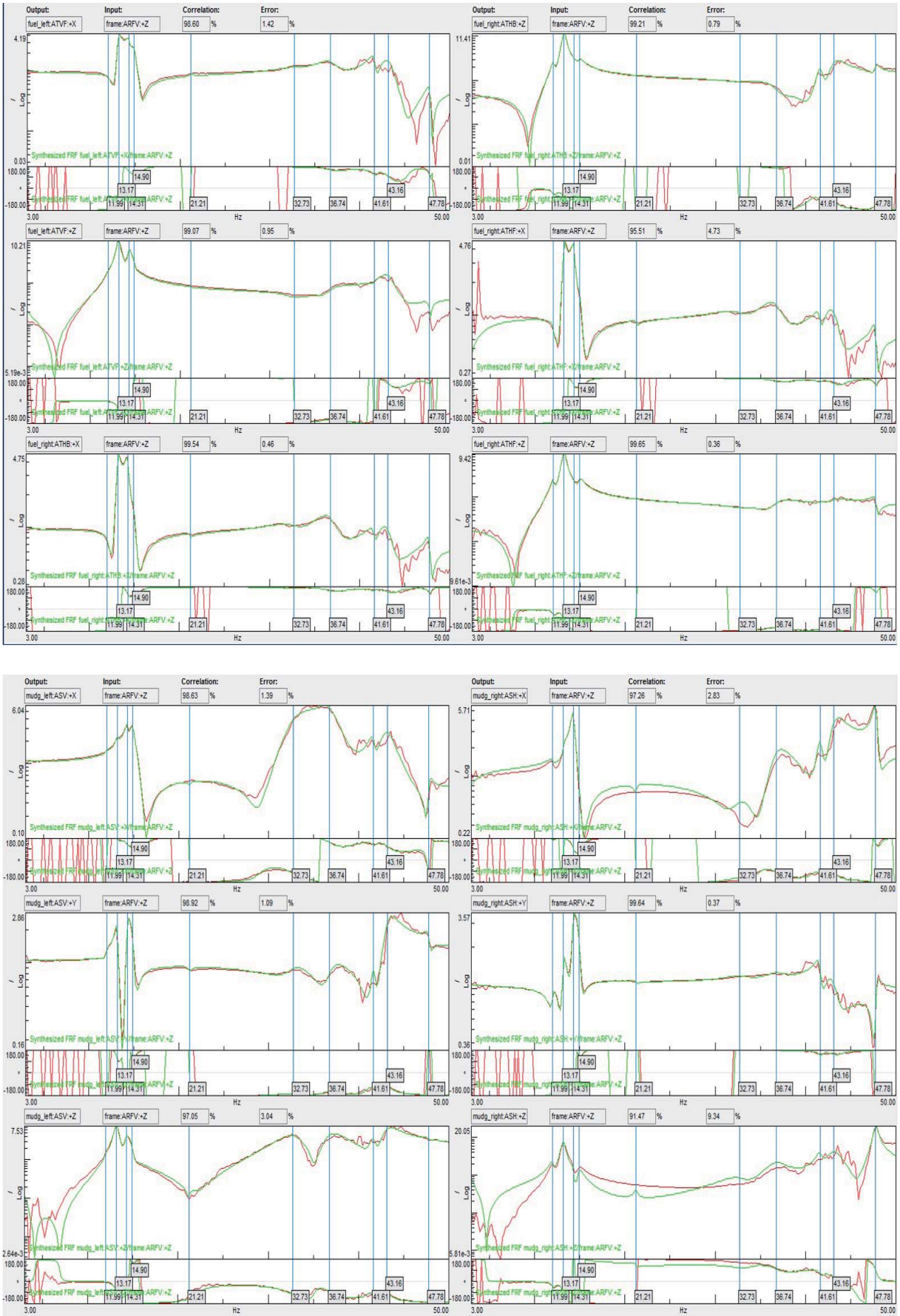

Figure 31: Synthesized FRFs

11.2.2 ARFHZ

In Table 10 the modal parameters are shown. Figure 32 shows the obtained stabilization diagram. Figure 33, 34 and 34 shows amplitude plots of the measured(red) and synthesized(green) FRFs.

Table 10: Identified modal parameters using *ARFHZ* as reference.

Mode No.	Undamped natural frequency	Modal damping ratio	Mode shape description
1	12.10 Hz	1.57 %	Excitation left fuel tank, z
2	13.25 Hz	1.37 %	Excitation both fuel tanks, z
3	14 Hz	1.85 %	Excitation right fuel tank, z
4	15.10 Hz	2.08 %	Excitation right fuel tank, z
5	21.22 Hz	1.23 %	Frame bending about z-axis
6	32.61 Hz	5.64 %	Excitation left mudguard bracket x and z
7	36.52 Hz	3.27 %	Excitation left mudguard bracket x and z
8	41.13 Hz	1.60 %	Frame bending about y-axis
9	44.51 Hz	2.09 %	Frame bending about y-axis
10	47.43 Hz	0.586491 %	Excitation right mudguard bracket z

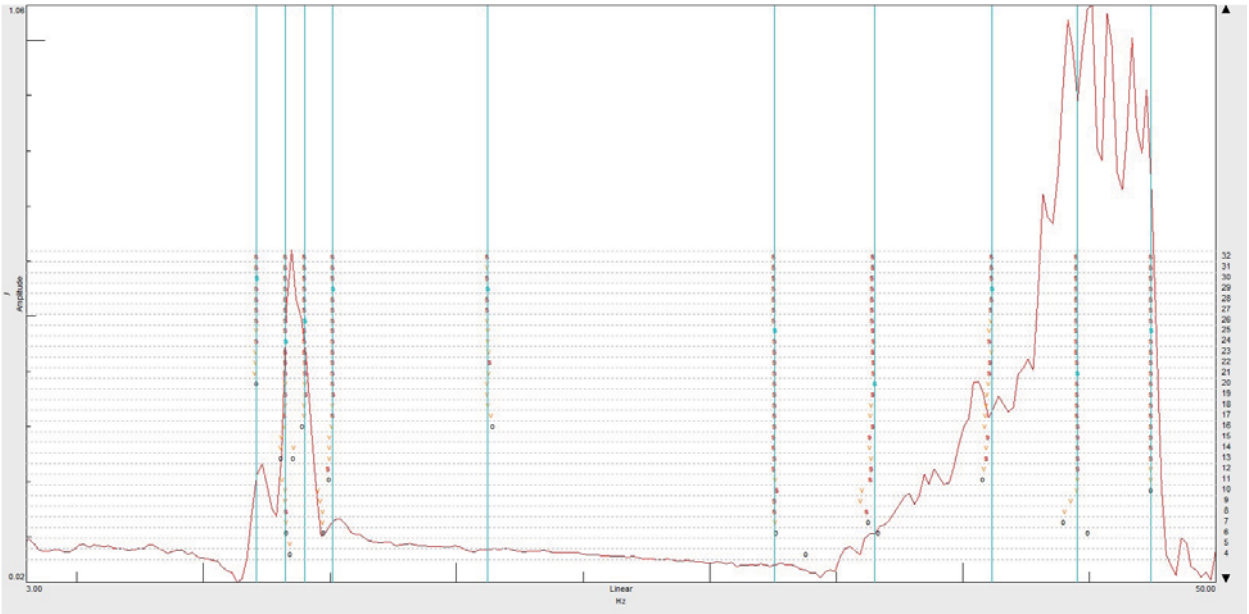

Figure 32: Stabilization diagram. The red curves shows the sum of used FRFs, model size N is indicated on the right hand side, s denotes stable reoccurring modes.

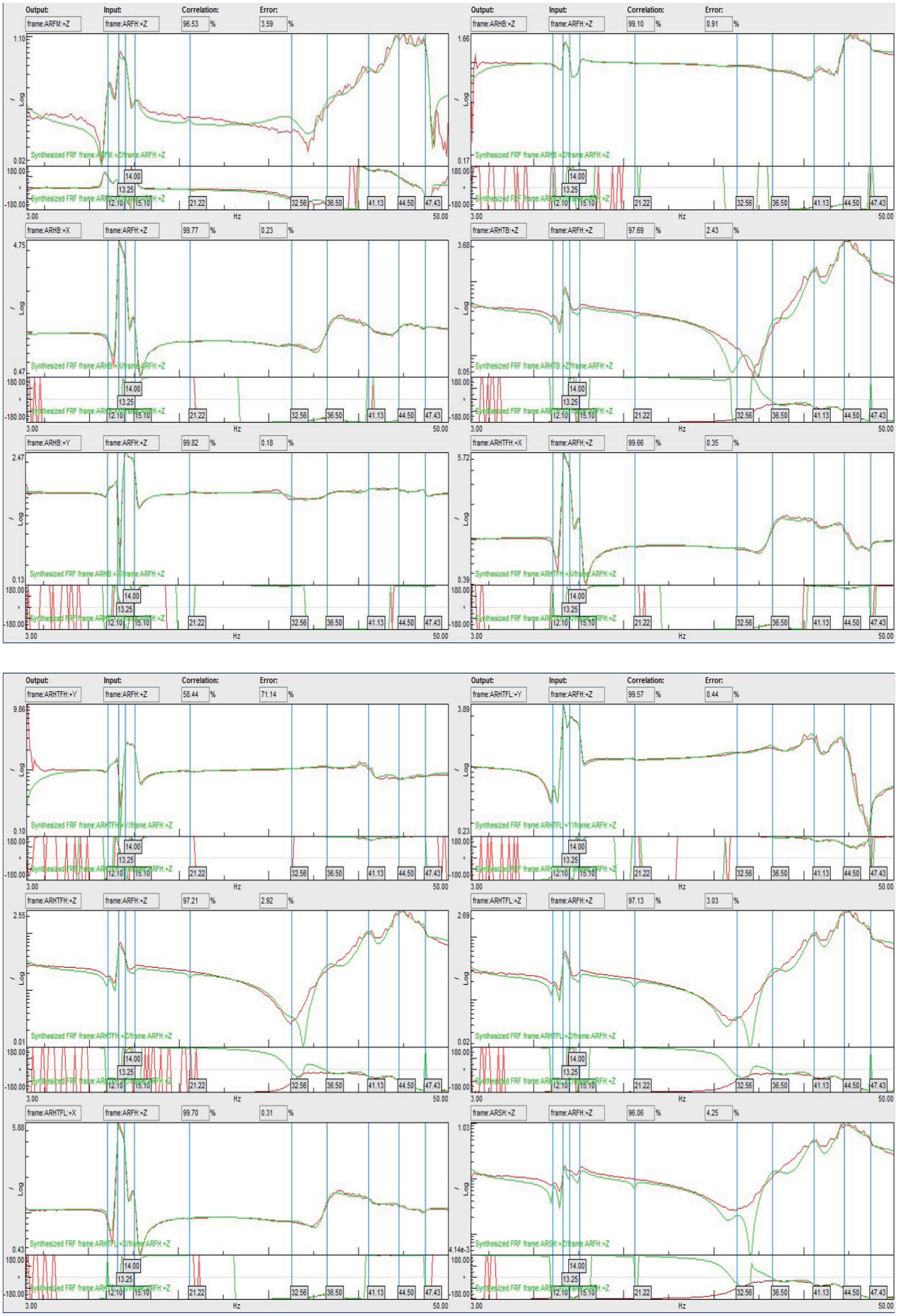

Figure 33: Sythesized FRFs.

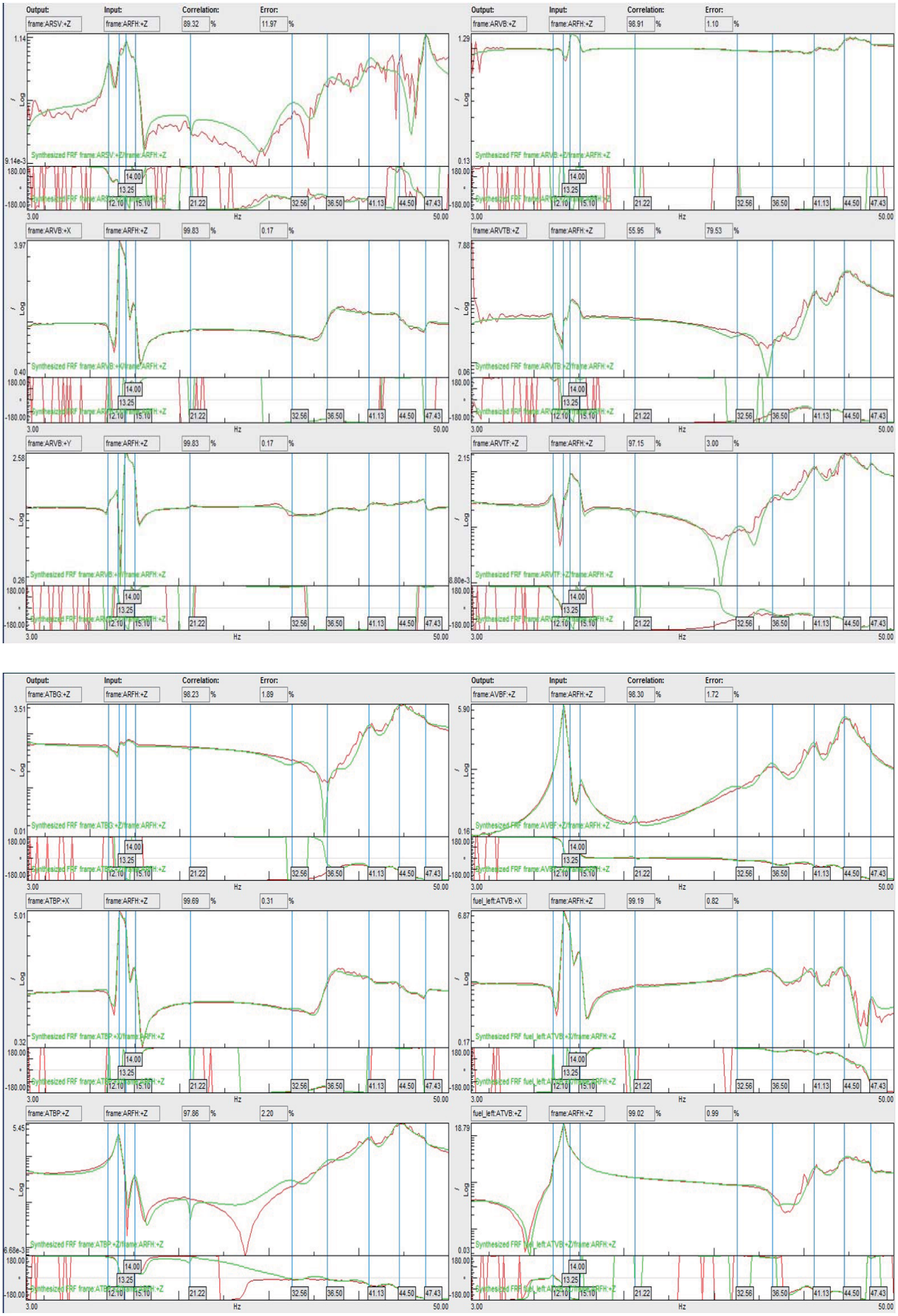

Figure 34: Sythesized FRFs.

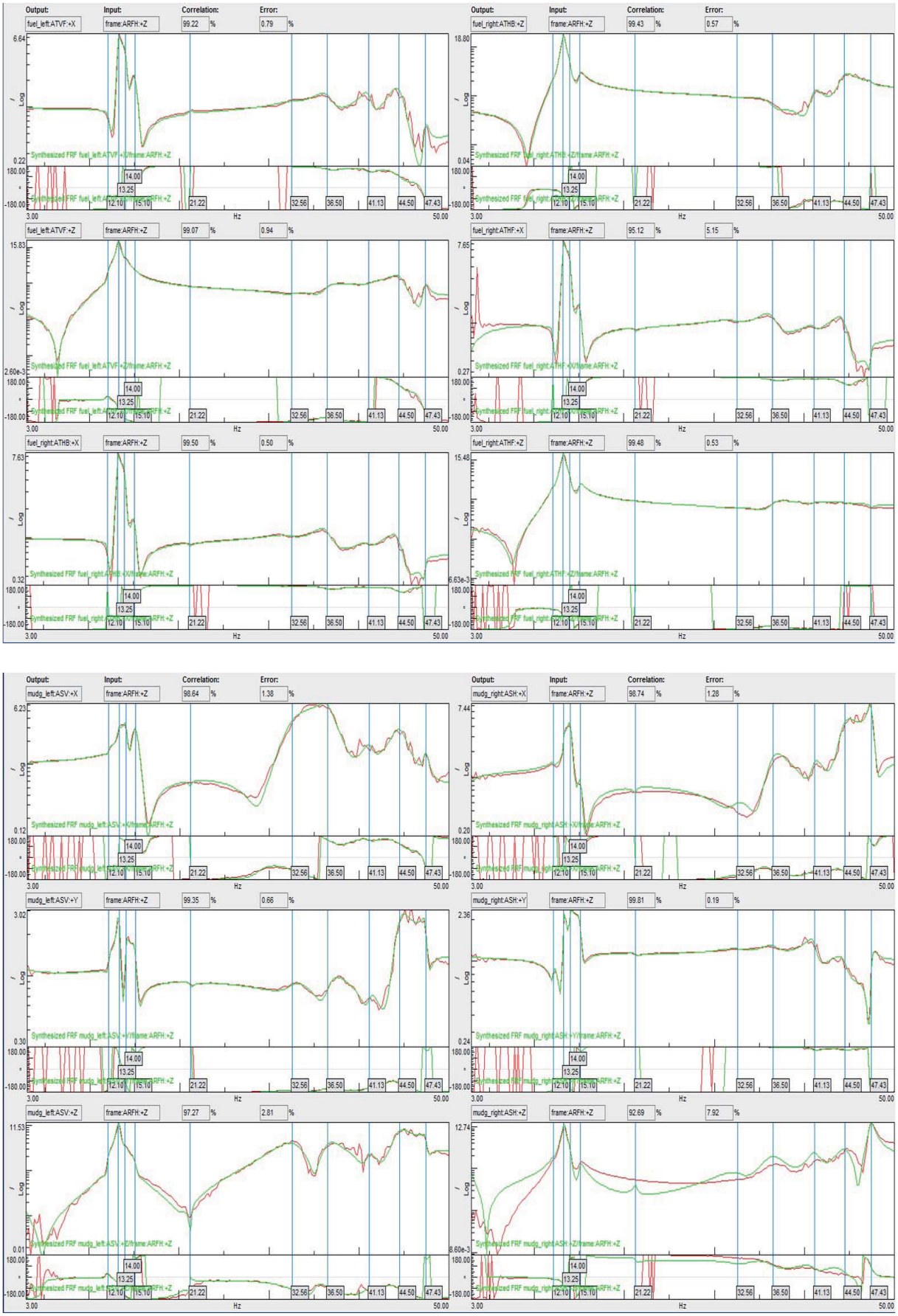

Figure 35: Sythesized FRFs.

11.3 Appendix C

In the following figures the resulting mode shapes from calculation of the undamped eigenvalue solution for each of the three MBS-models is depicted. The deformation is scaled to make the mode shapes clearer. The color shows relative deformation, where red indicates larger deformation and blue smaller deformation.

Note in Model 1 the deformation of the rubber suspended left mudguard bracket in mode one to four. Note also how mode eight and mode nine are dominated by the deformation of the left and right mudguard bracket respectively.

Comparing the modes of Model 1 and Model 2 it is evident that the mode shapes of the models are very similar.

Studying the mode shapes of Model 3 they are similar to those of Model 1 and Model 2, though the relative deformation differs. Mode eight in Model 3 corresponds to mode six in Model 1 and Model 2.

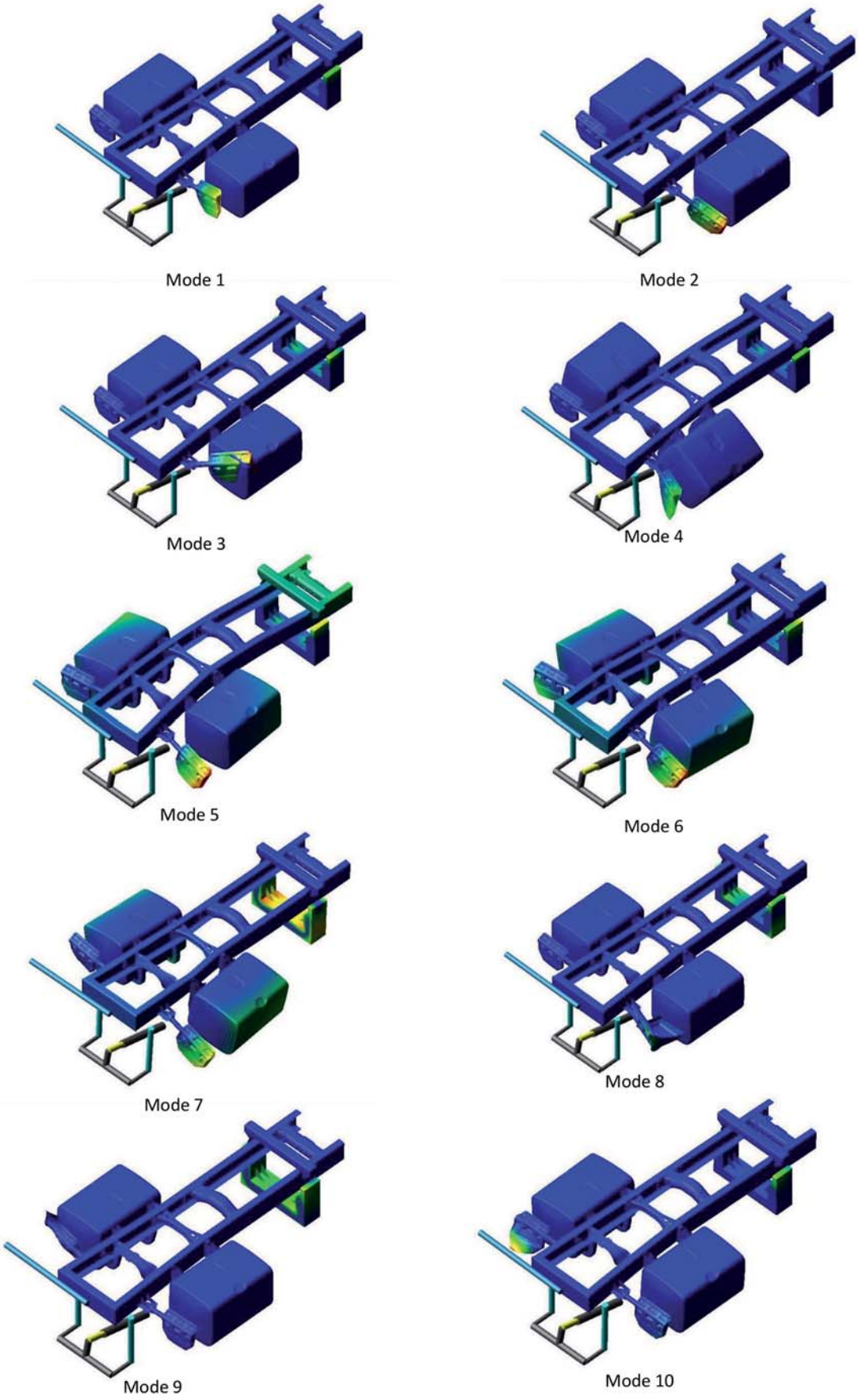

Figure 36: Mode shapes 1-10 for MBS Model 1.

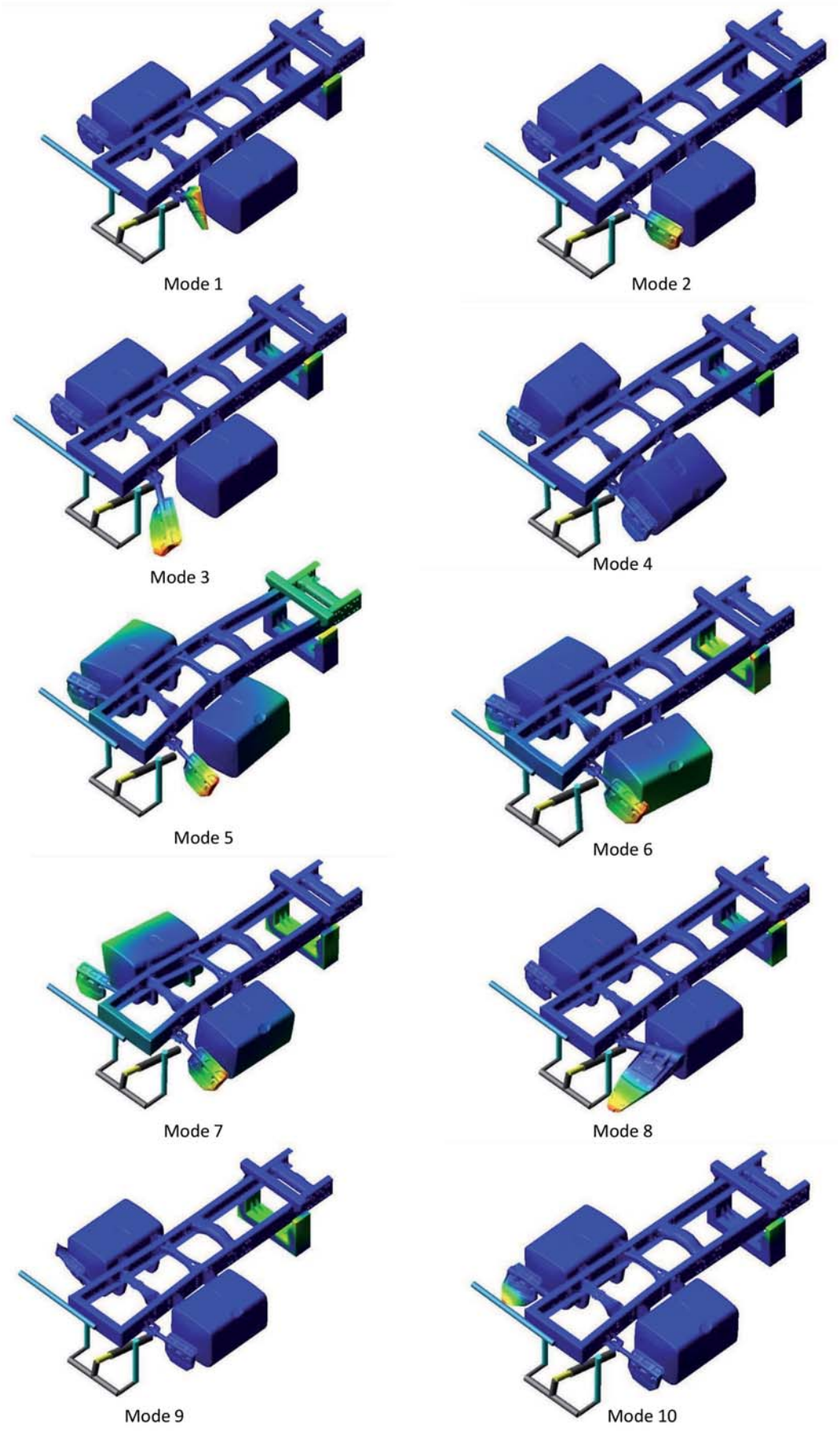

Figure 37: Mode shapes 1-10 for MBS Model 2.

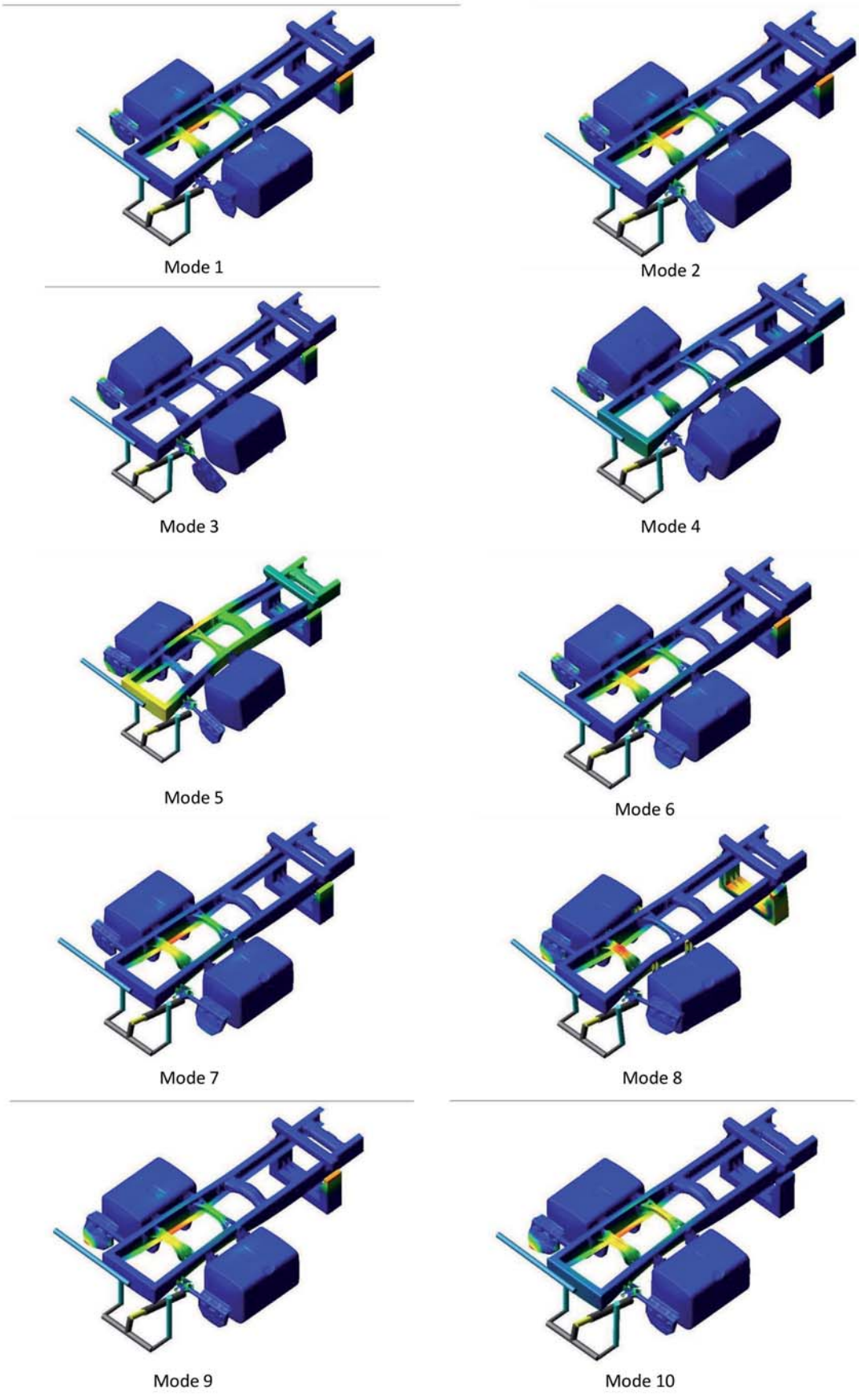

Figure 38: Mode shapes 1-10 for MBS Model 3.